

## IDENTIFYING LENSES WITH SMALL-SCALE STRUCTURE. II. FOLD LENSES

CHARLES R. KEETON<sup>1</sup>, B. SCOTT GAUDI<sup>2</sup>, AND A. O. PETTERS<sup>3,4</sup>

*Submitted to ApJ*

### ABSTRACT

When the light source in a four-image gravitational lens system lies sufficiently close to a “fold” caustic, two of the lensed images will lie very close together. If the lens potential is smooth on the scale of the separation between the two close images, then the difference between their fluxes should approximately vanish,  $R_{\text{fold}} \equiv (F_1 - F_2)/(F_1 + F_2) \approx 0$ . Violations of this “fold relation” in observed lenses are thought to indicate the presence of structure on scales smaller than the separation between the close images. We present a detailed study of the fold relation in realistic smooth lenses, finding it to be more subtle and rich than was previously realized. The degree to which  $R_{\text{fold}}$  can differ from zero for smooth lenses depends not only on the distance of the source from the caustic, but also on its location *along* the caustic, and then on the angular structure of the lens potential (ellipticity, multipole modes, and external shear). Since the source position is unobservable, it is impossible to say from  $R_{\text{fold}}$  alone whether the flux ratios in an observed lens are anomalous or not. Instead, we must consider the full distribution of  $R_{\text{fold}}$  values that can be obtained from smooth lens potentials that reproduce the separation  $d_1$  between the two close images and the distance  $d_2$  to the next nearest image. (By reducing the image configuration to these two numbers, we limit our model dependence and obtain a generic analysis.) We show that the generic features of this distribution can be understood, which means that the fold relation provides a robust probe of small-scale structure in lens galaxies. We then compute the full distribution using Monte Carlo simulations of realistic smooth lenses. Comparing these predictions with the data, we find that five of the 12 known lenses with fold configurations have flux ratio anomalies: B0712+472, SDSS 0924+0219, PG 1115+080, B1555+375, and B1933+503. Combining this with our previous analysis revealing anomalies in three of the four known lenses with cusp configurations, we conclude that *at least half (8/16) of all four-image lenses that admit generic, local analyses exhibit flux ratio anomalies*. The fold and cusp relations do not reveal the nature of the implied small-scale structure, but do provide the formal foundation for substructure studies, and also indicate which lenses deserve further study. Although our focus is on close pairs of images, we show that the fold relation can be used — with great care — to analyze all image pairs in all 22 known four-image lenses and reveal lenses with some sort of interesting structure.

*Subject headings:* cosmology: theory — dark matter — galaxies: formation — gravitational lensing — large-scale structure of universe

### 1. INTRODUCTION

Once baffling, the flux ratios between the images in four-image gravitational lens systems have recently become a source of considerable excitement. During the 1990s, standard lens models (using ellipsoidal lens galaxies, plus tidal shear from lens environments) successfully handled ever-improving data on the number and relative positions of lensed images, but consistently failed to fit the image fluxes. The first step toward solving this problem came when Mao & Schneider (1998) realized that small-scale structure in lens galaxies, which had previously been neglected, could easily explain the so-called “anomalous” flux ratios. The excitement began in earnest when Metcalf & Madau (2001) and Chiba (2002) pointed out that the Cold Dark Matter (CDM) paradigm might naturally explain the sort of substructure required to fit the fluxes. Soon after, Dalal & Kochanek (2002) introduced a method of analyzing lens data to measure the properties of substructure. They concluded that  $2.0^{+5.0}_{-1.4}$  percent (at 90% confidence) of the mass in lens galaxies is contained in substructure, which seemed to agree with CDM predictions, and

to reveal that the so-called “missing” satellites (Moore et al. 1999; Klypin et al. 1999) are in fact present but dark. Anomalous flux ratios had become a powerful test of CDM on small scales, and potentially a unique probe of the fundamental nature of dark matter.

Before carrying the conclusions too far, though, we must recall that there are many links in the chain of logic from observations of flux ratio anomalies to tests of CDM that need to be filled in. First, we must identify lenses with anomalous flux ratios. Second, we should list all the different types of small-scale structure<sup>5</sup> that might create flux ratio anomalies, and understand what observations or analyses could distinguish between them. Third, we must see if present data do distinguish different types of small-scale structure. If so, we can then quantify the amount of small-scale structure present in real lens galaxies. By comparing the inferred nature and abundance of small-scale structure to theoretical predictions, we can test the CDM paradigm. Finally, if we can understand how the predictions depend on the assumption that dark matter is cold and collisionless, we may be able to use lensing to probe the fundamental properties of the dark matter particle.

Dalal & Kochanek (2002) were the first to construct a realization of the full chain of logic. Briefly, they identified

<sup>1</sup> Department of Physics & Astronomy, Rutgers University, 136 Frelinghuysen Road, Piscataway, NJ 08837; keeton@physics.rutgers.edu

<sup>2</sup> Harvard-Smithsonian Center for Astrophysics, 60 Garden Street, Cambridge, MA 02138; sgaudi@cfa.harvard.edu

<sup>3</sup> Departments of Mathematics and Physics, Duke University, Durham, NC 27708; petters@math.duke.edu

<sup>4</sup> Bass Fellow

<sup>5</sup> The term “substructure” seems to have come to represent the sort of small-scale structure predicted by CDM. The term “small-scale structure” encompasses more general sorts of structure, and is our term of choice.

anomalous flux ratios as those that could not be fit with standard lens models. They focused on radio flux ratios in order to ignore microstructure associated with individual stars in lens galaxies, and assumed that the only important small-scale structure is dark matter clumps of the sort predicted by CDM. (They argued that other sorts of small-scale structure, such as globular clusters and dwarf galaxies, are much less abundant than the inferred number of CDM clumps.) They assumed that amount of CDM substructure is a universal fraction of the total density, used the lens observations to place constraints on that fraction, and then compared their results with predictions from CDM simulations. Making the various assumptions was necessary to build the first connection between lens flux ratios and the nature of dark matter. However, questions have been raised about some of them, which prompt us to go back and reassess each link in the chain. This evaluation is essential if we want to claim lensing as a reliable probe of small-scale structure in the universe. Moreover, it is intrinsically interesting because it will lead us to a deeper understanding of diverse topics in both lensing and structure formation theory.

Let us first consider the CDM end of the chain. A lot of recent effort has gone into refining predictions about substructure. It now appears that the substructure mass fraction need not be universal, but may vary both within a given halo and from one halo to another (e.g., Chen et al. 2003; Zentner & Bullock 2003; Mao et al. 2004; Oguri & Lee 2004). Tidal forces might be able to destroy dark matter clumps at the small radii where lensed images typically appear, in which case CDM might predict *too little* substructure to explain observed flux ratio anomalies (Mao et al. 2004; Amara et al. 2004). If this really is a problem, one possible solution is that small halos projected along the line of sight could bring the total amount of small-scale structure back up to the level that seems to be required by lensing (Keeton 2003; Chen et al. 2003; Metcalf 2004a,b). Another possibility is that revised analyses of lens data may lower the required amount of small-scale structure (see below). A third possibility, of course, is that lensing and CDM simply disagree about small-scale structure. In any case, the important point is that the CDM predictions are challenging and still somewhat uncertain, and more work needs to be done. Mastering the theory involves both technical issues (numerical resolution) and physical effects (dynamical friction, tidal disruption), so it is not only essential for interpreting the lensing results, but also interesting in its own right.

Now moving to the lensing side, we must first ask whether flux ratio anomalies are real. Evans & Witt (2003) recently suggested that at least some of the “anomalies” might just be artifacts of certain assumptions in standard lens models. Specifically, instead of assuming the usual elliptical symmetry, they allowed perturbations from  $m=3$  and  $m=4$  multipole modes. Such modes are not only observed in the luminosity distributions of real galaxies (Bender et al. 1989; Saglia et al. 1993; Rest et al. 2001), but also predicted in the mass distributions of simulated galaxies (Heyl et al. 1994; Naab & Burkert 2003), so it does not seem crazy to allow them in lens models. Evans & Witt found that they could fit two of the three “anomalous” lenses they considered, without substructure. In response, Kochanek & Dalal (2004) argued that even if  $m=3,4$  multipole modes might explain individual lenses, they cannot explain an important statistical property of the ensemble of flux ratio anomalies: an asymmetry between images that form at minima of the time delay surface

and those that form at saddle points, such that anomalous minima are almost always brighter than expected while anomalous saddles are usually fainter than expected. To its credit, the CDM substructure hypothesis, and stellar microlensing, can both explain such an asymmetry (Metcalf & Madau 2001; Schechter & Wambsganss 2002; Keeton 2003; Bradač et al. 2004). However, it is not yet known whether alternative hypotheses could explain the asymmetry as well. In a different response to Evans & Witt, Yoo et al. (2005) recently showed that in PG 1115+080 the Einstein ring image of the quasar host galaxy rules out the sorts of multipole modes that would be needed to fit the quasar flux ratios. This type of analysis is very promising, but it demands deep, high-resolution, near-infrared observations combined with a sophisticated modeling analysis, and it must be applied on a case-by-case basis.

Clearly, a top priority must be to develop methods to determine whether flux ratio anomalies are real and indicate small-scale structure. One approach is to look for new data that cleanly reveal small-scale structure. The most unambiguous situation is the detection of flux perturbations associated with microlensing by stars in the lens galaxy. Detecting time variability in optical fluxes can prove that microlensing occurs (e.g., Woźniak et al. 2000; Schechter et al. 2003). Barring that, the next best thing is to take optical spectra of lensed images and use similarities or differences between emission line and continuum flux ratios to distinguish between microlensing, millilensing (a term sometimes applied to flux perturbations caused by CDM-type substructure), and errors in the macromodel (Moustakas & Metcalf 2003). The required observations are challenging, but the method does appear to be successful (Wisotzki et al. 2003; Metcalf et al. 2004; Morgan et al. 2004a; Wayth et al. 2005). At this point, it is appropriate to note that the “more data” program has made it possible to conclude that, whatever their lensing interpretation may be, flux ratio anomalies are not electromagnetic phenomena. Measurements of flux ratios at a variety of wavelengths have shown that differential extinction and scattering cannot explain the unusual observed flux ratios (see Kochanek & Dalal 2004, and Appendix B).

An alternate approach is to reanalyze data that are already in hand. Traditionally, flux ratio anomalies have been identified as those that cannot be fit with certain smooth lens models (e.g., Dalal & Kochanek 2002; Metcalf & Zhao 2002; Kochanek & Dalal 2004). That analysis is, of course, susceptible to the criticism of being model-dependent. Perhaps even more important, it may be sensitive to certain global symmetries in the popular lens models that lead to global relations among the magnifications of the four images (Dalal 1998; Witt & Mao 2000; Hunter & Evans 2001; Evans & Hunter 2002). Failure to fit observed flux ratios may simply indicate failure of the global symmetries — which is very different from saying that there must be small-scale structure. To circumvent both of these problems, we would like to develop an analysis that is both *local* in the sense that it only depends on properties of the lens potential around and between closely-spaced images, and *generic* in the sense that it does not depend on any specific properties of the types of models that are used to analyze the data.

Fortunately, lens theory has uncovered precisely what we need: local and generic relations between the magnifications between certain images in certain configurations. Specifically, two images in a “fold pair” (defined in §2) should have  $|\mu_A| - |\mu_B| \approx 0$ , while three images in a “cusp triplet” should have  $|\mu_A| - |\mu_B| + |\mu_C| \approx 0$ . This cusp relation played a central

role in the analysis by Mao & Schneider (1998) that led to the idea that lens flux ratios may probe small-scale structure. If we want to use the fold and cusp relations today, however, we must rigorously understand how “local” and “generic” they really are, and whether they can actually be used as the basis of a realistic but robust method for identifying flux ratio anomalies that indicate small-scale structure.

The standard fold and cusp relations are derived from low-order Taylor series expansions in the vicinity of a fold or cusp caustic (Mao 1992; Schneider & Weiss 1992; Schneider et al. 1992; Petters et al. 2001; Gaudi & Petters 2002a,b). Formally, they are only valid when the source lies asymptotically close to a caustic. We have undertaken to reexamine the relations in more realistic settings, when the source sits a small but finite distance from a caustic, and the lens potential has a variety of nontrivial but smooth structures such as different radial profiles, ellipticities, octopole ( $m = 4$ ) modes, and external tidal shears. In Keeton et al. (2003, hereafter Paper I), we studied the cusp relation. We found it to be insensitive to the radial profile of the lens galaxy, but quite sensitive to ellipticity, multipole modes, and shear. We quantified the degree to which these features can cause  $|\mu_A| - |\mu_B| + |\mu_C|$  to deviate from zero even for smooth lenses. We then compared those allowed deviations with observed data and found that five observed lenses violate the realistic cusp relation in ways that indicate the presence of small-scale structure (B0712+472, RX J0911+0551, SDSS 0924+0219, RX J1131–1231, and B2045+265). We were very careful to state the limitations of the analysis, in particular to remark that study of the cusp relation — like all other analyses of single-epoch, single-band flux ratios — cannot reveal the nature of the implied small-scale structure. The strongest conclusion that can be drawn from a generic analysis is that the lens must have significant structure on scales smaller than the separation between the triplet of cusp images. We believe that this sort of deep discussion of the general features and applicability of a generic magnification relation is as valuable as the specific identification of flux ratio anomalies that it allows.

In this paper, we turn our attention to the fold relation. We again seek to understand the general properties of the relation in realistic situations, and to use that understanding to identify violations of the fold relation. We adopt the same basic approach as in Paper I: we first examine simple lens potentials analytically, then develop a Monte Carlo approach to study the fold relation in a realistic lens population, and finally use the realistic fold relation to look for flux ratio anomalies in observed lenses. However, many fine points of the discussion are rather different, because there are subtle but important ways in which the fold and cusp relations behave differently. In addition, we have come to understand that the fold relation may be used — with great care — to learn something interesting about image pairs that are not obviously fold pairs. The discussion of observed lenses therefore has a somewhat larger scope in this paper than it did in Paper I. One final difference is that the sample of published four-image lenses has grown by three since Paper I.

As in Paper I, we assert that, even though we adopt specific families of lens potentials, our analysis is more general than explicit modeling. One reason is that we take great pains to understand what is generic in the fold relation. A second reason is that we have a better distinction between global and local properties of the lens potential. For example, a global  $m = 1$  mode (i.e., a lack of reflection symmetry) would affect conclusions about anomalies in direct modeling, but not in our

analysis. A third point is that our results are less *modeling* dependent, less subject to the intricacies of fitting data and using optimization routines. A fourth advantage of our analysis is that, rather than simply showing the standard models fail to fit a lens, it clearly diagnoses why. We believe that these benefits go a long way toward establishing that small-scale structure in lens galaxies is real and can be understood.

We must again address a question that is semantic but important: Where do we draw the line between a normal “smooth” lens potential and “small-scale structure”? As in Paper I, we take a pragmatic approach and consider “smooth” lenses to include anything that is known to be common in galaxies, especially early-type galaxies: certain radial density profiles, reasonable ellipticities, small octopole modes representing disky or boxy isophotes, and moderate tidal shears from lens environments. Finding evidence for any or all of those in any given lens would not cause much stir. We then consider “small-scale structure” to be anything whose presence in lens galaxies would be notable and worthy of further study. In other words, we do not attempt to distinguish between microlensing, CDM-type substructure, massive and offset disk components, large-amplitude or intermediate-scale multipole modes, etc. as explanations for flux ratio anomalies. That is properly the subject of a separate analysis, which can begin only once flux ratio anomalies have been rigorously identified.

The organization of the paper is as follows. We begin in §2 by introducing a way to quantify four-image lens configurations that is convenient for the fold relation. In §3 we review the ideal magnification relations for folds and cusps. In §4 we use a simple lens potential to examine the general properties of the fold relation in different regimes. In §5 we introduce a Monte Carlo technique for characterizing the fold relation for a realistic population of lens potentials. In §6 we use our understanding of the fold relation to evaluate all of the observed four-image lenses. We offer our conclusions and discussion in §7. Two appendices provide supporting technical material. In Appendix A we present an important extension of the usual Taylor series analysis leading to the fold relation. In Appendix B we summarize the data that we analyze for all of the published four-image lenses.

## 2. CHARACTERIZING FOUR-IMAGE LENSES

At least 23 quadruply imaged lens systems are known. This count includes the 10-image system B1933+503, which is complex because there are two different sources that are quadruply imaged and a third that is doubly imaged (Sykes et al. 1998). It excludes PMN J0134–0931 and B1359+154 because each system has multiple lens galaxies that lead to image multiplicities larger than four (Rusin et al. 2001; Keeton & Winn 2003; Winn et al. 2003). The count also excludes systems like Q0957+561 in which some faint secondary features — including the host galaxy of the source quasar — may be quadruply imaged but are difficult to study (Bernstein et al. 1997; Keeton et al. 2000). Published data for the quadruply imaged systems are reviewed in Appendix B.

The image configurations of quad lenses can usually be classified “by eye” into three categories: folds, cusps,<sup>6</sup> and crosses. The names are related to the location of the source with respect to the lensing caustics. For our purposes it is

<sup>6</sup> Some authors subdivide cusps depending on whether they are associated with the long or short axis of the lens potential (e.g., Saha & Williams 2003), and we will follow suit when convenient.

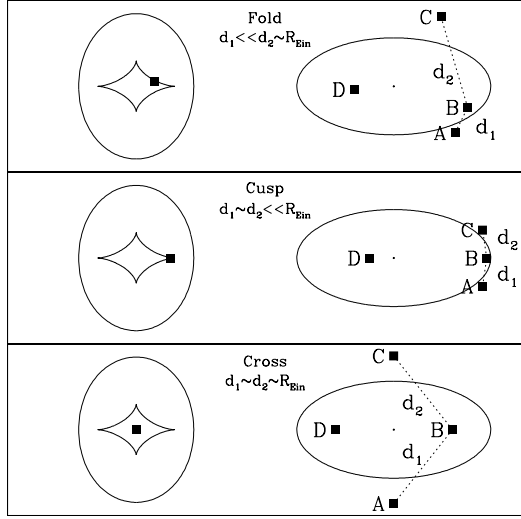


FIG. 1.— Three fiducial configurations of four-image lenses: fold (top), cusp (middle), and cross (bottom). In each panel, the figure on the left shows the caustics and source position in the light source plane, while the figure on the right shows the critical curves and image positions in the image plane. Despite appearances, the fold and cusp sources sit a finite distance from the caustic. The configurations are distinguished by the distances  $d_1$  and  $d_2$ , as indicated.

more important to find a simple but quantitative way to characterize the configurations. When studying cusp lenses in Paper I, we used the separation and opening angle of a triplet of images. To study fold configurations, we are interested in pairs of images, in particular pairs comprising one image at a minimum of the time delay surface and one at a saddle point. (The parities of the images can usually be determined unambiguously; see Saha & Williams 2003.) Let us label the two minima  $M_1$  and  $M_2$ , and the two saddles  $S_1$  and  $S_2$ . When considering the pair  $M_1S_1$ , for example, we define  $d_1 = D(M_1, S_1)$  and  $d_2 = \min[D(M_1, S_2), D(M_2, S_1)]$ , where  $D(i, j)$  is the distance between images  $i$  and  $j$ . In other words,  $d_1$  is the separation between the images for the pair in question, and  $d_2$  is the distance to the next nearest image. Note that  $d_1$  and  $d_2$  describe a *pair* of images. At times it is convenient to characterize the full configuration of all four images, and we define  $d_1^*$  and  $d_2^*$  to be the values of  $d_1$  and  $d_2$  for the pair with the smallest separation. (The context will make clear whether we are using  $d_1$  and  $d_2$  or  $d_1^*$  and  $d_2^*$ .)

Figure 1 illustrates the three fiducial configurations, and indicates  $d_1$  and  $d_2$  for sample image pairs. In a fold lens, the source sits near a fold caustic so two of the images lie close together with  $d_1 \ll d_2$ . Furthermore,  $d_2$  is comparable to the other scale in the problem, the Einstein radius  $R_{\text{ein}}$ . In a cusp lens, the source is near a cusp caustic so three of the images are close together and we have  $d_1 \sim d_2 \ll R_{\text{ein}}$ . If the source does not lie near a caustic, then the images form a relatively symmetric cross configuration with  $d_1 \sim d_2 \sim R_{\text{ein}}$ .

Incidentally, for the three “archetypal” image configurations shown in Figure 1, we have chosen the source positions so that  $d_1^{\text{fold}} = d_1^{\text{cusp}} = d_2^{\text{cusp}}$  while  $d_2^{\text{fold}} = d_1^{\text{cross}} = d_2^{\text{cross}}$ . This means we can smoothly morph from the fold to the cusp by fixing  $d_1$  and varying  $d_2$ , or from the fold to the cross by fixing  $d_2$  and varying  $d_1$ .

### 3. ASYMPTOTIC MAGNIFICATION RELATIONS FOR FOLDS AND CUSPS

In this section we briefly review the expected relations between the magnifications of images corresponding to a source near a fold or cusp caustic. As Paper I discussed in depth, when the source lies near a cusp caustic, the three associated images should have<sup>7</sup>

$$R_{\text{cusp}} \equiv \frac{|\mu_A| - |\mu_B| + |\mu_C|}{|\mu_A| + |\mu_B| + |\mu_C|} = \frac{F_A - F_B + F_C}{F_A + F_B + F_C} \approx 0, \quad (1)$$

where  $\mu_i$  is the signed magnification of image  $i$ , while  $F_i = F_{\text{src}}|\mu_i|$  is the flux of the image if the source has flux  $F_{\text{src}}$ . ( $R_{\text{cusp}}$  is defined such that it is independent of  $F_{\text{src}}$ .) In our naming convention, B is the middle of the three images and there is no need to specify whether it is a minimum or saddle image. To state eq. (1) more precisely, we expand the lens mapping in a Taylor series about the cusp and find  $R_{\text{cusp}} = 0 + A_{\text{cusp}}d^2 + \dots$ , where  $d$  is the maximum separation between the three images. The constant and linear terms in the expansion vanish, so when the source is sufficiently close to the cusp (such that  $d \rightarrow 0$ ),  $R_{\text{fold}}$  should vanish independent of any properties of the lens potential (apart from the condition that a cusp caustic exists). However, when the source lies a small but finite distance from the cusp, there is a correction term at second order in  $d$ , whose coefficient  $A_{\text{cusp}}$  does depend on properties of the lens potential — namely, the ellipticity, external shear, and any higher order multipole modes that may be present. Nevertheless, for realistic distributions of those quantities it is possible to derive reliable upper bounds on  $R_{\text{cusp}}$ . Roughly speaking, we may say that those bounds can be violated only if the lens potential has significant structure on scales smaller than the distance between images, although Paper I provides a much more careful discussion.

Appendix A of this paper shows that when the source lies near a fold caustic, the two images near the fold critical point should have

$$R_{\text{fold}} \equiv \frac{|\mu_{\text{min}}| - |\mu_{\text{sad}}|}{|\mu_{\text{min}}| + |\mu_{\text{sad}}|} = \frac{F_{\text{min}} - F_{\text{sad}}}{F_{\text{min}} + F_{\text{sad}}} \approx 0. \quad (2)$$

We are interested in pairs consisting of a minimum and a saddle, and we define  $R_{\text{fold}}$  such that the saddle image gets the minus sign in the numerator. Again, to be more precise we use a Taylor series expansion of the lens mapping near the fold point to find  $R_{\text{fold}} = 0 + A_{\text{fold}}d_1 + \dots$ , where  $d_1$  is the distance between the two images. The ideal fold relation  $R_{\text{fold}} \approx 0$  holds only when the source is asymptotically close to the caustic. Now there is a correction term at first order in  $d_1$ , whose coefficient  $A_{\text{fold}}$  depends on properties of the lens potential (see eq. A21 in Appendix A). In other words, the correction to the fold relation is of lower order than the correction to the cusp relation, which means that the fold relation is more sensitive to a small offset from the caustic. Thus, some care will be needed to determine whether an observed violation of the ideal fold relation really reveals small-scale structure, or just indicates that the source lies a finite distance from a fold caustic.

### 4. UNDERSTANDING THE FOLD RELATION

#### 4.1. In the asymptotic regime

<sup>7</sup> In Paper I we used the absolute value of  $R_{\text{cusp}}$ , but it has become clear that the sign is an important component of theoretical predictions (e.g., Metcalf & Madau 2001; Schechter & Wambsganss 2002; Keeton 2003; Kochanek & Dalal 2004; Bradač et al. 2004) so we retain it now. Working with the signed quantity would not change the conclusions of Paper I.

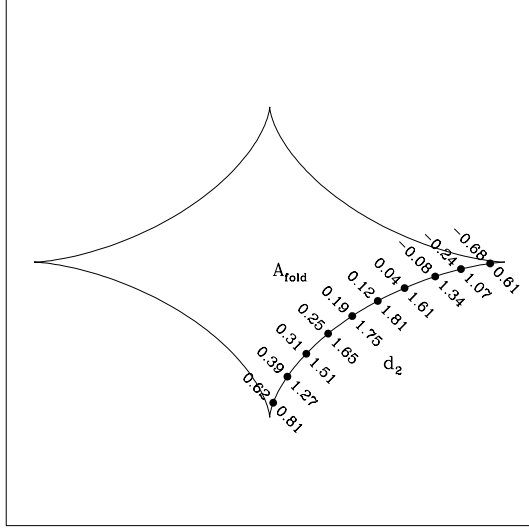


FIG. 2.— Caustic curve for an isothermal ellipsoid lens with ellipticity  $e = 0.5$ . The numbers above the points indicate values of the coefficient  $A_{\text{fold}}$  in the asymptotic fold relation  $R_{\text{fold}} = A_{\text{fold}} d_1 + \dots$  at various points along the caustic. (See eq. A21 in Appendix A; recall that  $A_{\text{fold}}$  is to be evaluated *on* the caustic, but it then describes the fold relation in the *vicinity* of the caustic.) The numbers below the points indicate the corresponding values of  $d_2$  (in units with  $R_{\text{ein}} = 1$ ). The other quadrants can be filled in by symmetry.

We can begin to understand general features of the fold relation by examining the coefficient in the asymptotic limit for  $R_{\text{fold}}$ ,

$$A_{\text{fold}} = \frac{3\psi_{122}^2 - 3\psi_{112}\psi_{222} + \psi_{2222}(1 - \psi_{11})}{6\psi_{222}(1 - \psi_{11})}, \quad (3)$$

where the  $\psi$ 's represent various derivatives of the lens potential, evaluated at the fold point (see eqs. A21–A23 in Appendix A). Imagine moving along the caustic and evaluating  $A_{\text{fold}}$  at various points. As we approach a cusp,  $\psi_{222} \rightarrow 0$  while the other derivatives remain finite (e.g., Petters et al. 2001, p. 346), so  $|A_{\text{fold}}| \rightarrow \infty$ . The sign depends on the type of cusp. A “positive” cusp has two minimum images and one saddle, and typically occurs on the long axis of the lens potential; it has  $A_{\text{fold}} \rightarrow -\infty$  with a minus sign because the saddle image is brighter than each minimum. A “negative” cusp has two saddles and one minimum, and typically occurs on the short axis of the potential; it has  $A_{\text{fold}} \rightarrow +\infty$  with a plus sign because the minimum image is brighter than each saddle. One implication of  $|A_{\text{fold}}| \rightarrow \infty$  is that the fold relation breaks down near a cusp, but that is not surprising because the asymptotic analysis in Appendix A explicitly assumes that we have chosen a fold point and are examining a small neighborhood that does not include a cusp point. Besides, near a cusp it is the cusp relation that ought to be satisfied, not the fold relation.

The more interesting implication is that  $A_{\text{fold}}$  can take on all real values, both positive and negative. Unless there is some remarkable discontinuity, there must be some region where  $A_{\text{fold}}$  changes sign. Figure 2 confirms that this is the case for a typical example (an isothermal ellipsoid lens with ellipticity  $e = 0.5$ ). There is a region where  $|A_{\text{fold}}|$  is small or even zero, so that the ideal fold relation  $R_{\text{fold}} \approx 0$  is quite a good approximation. In this region the distance  $d_2$  is large,<sup>8</sup> but

<sup>8</sup> The distance  $d_1$  can be arbitrarily small depending on how close the source is placed to the caustic, but  $d_2$  remains finite even when the source lies right on the caustic.

interestingly the smallest values of  $|A_{\text{fold}}|$  do not correspond to the largest values of  $d_2$ . Over the larger range where  $d_2$  is large enough that the image configuration would be classified as a fold (roughly  $d_2 \gtrsim 1$ ), we find  $|A_{\text{fold}}| \sim 0.1–0.3$ . The important implication is that a lot of lenses that are clearly folds may nevertheless fail to satisfy the ideal fold relation  $R_{\text{fold}} \approx 0$ .

An even more important conclusion is that the validity of the ideal fold relation depends not just on whether the source is close to a fold caustic, but where the source is located *along* the caustic. This point is shown more directly in the next subsection.

#### 4.2. Across the source plane

To move beyond the asymptotic regime, we use the software by Keeton (2001) to solve the lens equation exactly throughout source plane for an isothermal ellipsoid lens with ellipticity  $e = 0.5$ . For each source inside the astroid caustic, we find the four images, identify the pair with the smallest separation, and then compute  $d_1$ ,  $d_2$ , and  $R_{\text{fold}}$  for that pair. (These are by definition the same as  $d_1^*$  and  $d_2^*$ .) The results are shown in Figure 3. First, it is valuable to understand how  $d_1$  and  $d_2$  vary with source position, as shown in panels (a) and (b). The separation  $d_1$  between the images measures very directly the distance of the source from the caustic. The distance  $d_2$  to the next nearest image varies along the caustic, and basically measures the distance of the source from a cusp. In general, fixing both  $d_1$  and  $d_2$  fixes the source to one of eight positions (two in each quadrant).

Panels (c) and (d) show  $R_{\text{fold}}$  as a function of source position, with contours of  $d_1$  and  $d_2$  overlaid.  $R_{\text{fold}}$  is large and negative near the long-axis cusp, and it is large and positive in a band extending from one short-axis cusp to the other and passing through the origin. The area in which  $R_{\text{fold}} > 0$  is larger than the area in which  $R_{\text{fold}} < 0$ , which means that the distribution of  $R_{\text{fold}}$  values is not symmetric about  $R_{\text{fold}} = 0$ . Near the origin,  $R_{\text{fold}}$  is large and positive. Both of these points will be important for our analysis of real lenses in §6. There is a “wedge” of small  $R_{\text{fold}}$  values starting at the caustic but extending well inside; this corresponds to the region where the asymptotic coefficient  $A_{\text{fold}}$  is nearly zero (see Fig. 2). Interestingly, in the region near the caustic and midway between the cusps, where  $d_2$  is large and where we would expect to find archetypal folds,  $R_{\text{fold}}$  is not terribly small. The source must get very close to the caustic before  $R_{\text{fold}}$  vanishes. A remarkable visual impression is that  $R_{\text{fold}}$  seems to be more correlated with the  $d_2$  contours than with the  $d_1$  contours.

Finally, by tabulating the results for all the different source positions we can plot  $R_{\text{fold}}$  in the  $(d_1, d_2)$  plane, as shown in panels (e) and (f).<sup>9</sup> There are two plots because there are two source positions in each quadrant, and hence two values of  $R_{\text{fold}}$ , with the same values of  $d_1$  and  $d_2$ . These figures show more clearly that  $R_{\text{fold}}$  vanishes as  $d_1 \rightarrow 0$ , but the speed with which that occurs depends on the value of  $d_2$ . Furthermore, in the upper left corner (the region of fold configurations), the  $R_{\text{fold}}$  contours bend over and become quite sensitive to  $d_2$ .

We are forced to conclude that the fold relation depends not only on proximity to a fold caustic, but also on location along the caustic. Although we are not shocked — we knew that the fold relation should break down near a cusp — we are nevertheless surprised to discover how sensitive  $R_{\text{fold}}$  is to lo-

<sup>9</sup> We generated the figures with Monte Carlo sampling of the source plane, which yields imperfect sampling of the  $(d_1, d_2)$  plane in the lower left corner.

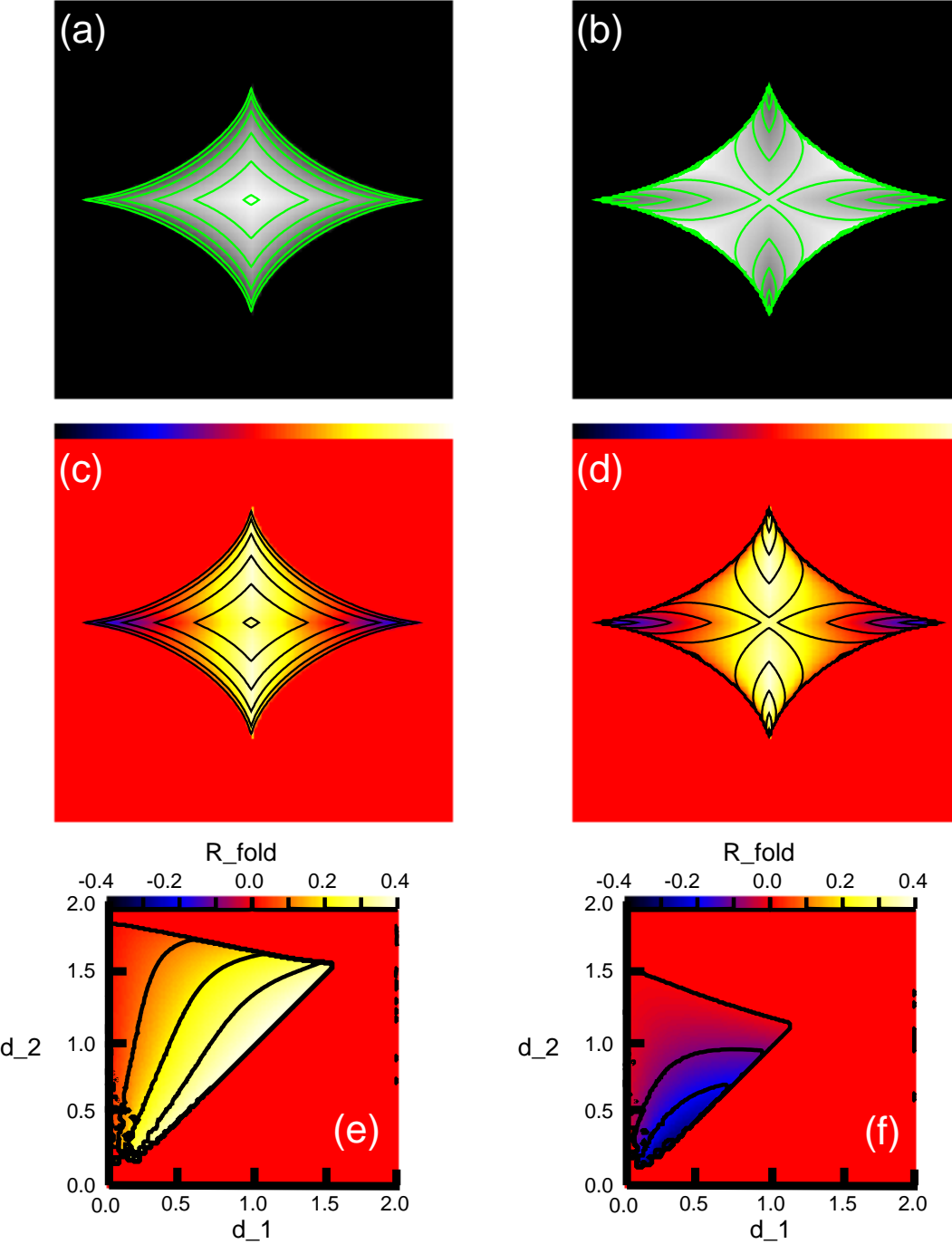


FIG. 3.— (a) The grayscale and contours both show the distance  $d_1$  as a function of source position, for an isothermal ellipsoid lens with ellipticity  $e = 0.5$ . The contours range from 0 to 1.5 in steps of 0.25, in units with  $R_{\text{ein}} = 1$ . (b) The distance  $d_2$  as a function of source position; the contours are again spaced by 0.25. (c) The colors show  $R_{\text{fold}}$  as a function of source position, going from black at  $R_{\text{fold}} \rightarrow -1$  through red at  $R_{\text{fold}} = 0$  to white at  $R_{\text{fold}} \rightarrow +1$ . The  $d_1$  contours from panel a are overlaid. (d) The colors again show  $R_{\text{fold}}$ , with the  $d_2$  contours from panel b now overlaid. (e-f) The colors and contours both show  $R_{\text{fold}}$  as a function of  $d_1$  on the abscissa and  $d_2$  on the ordinate; the contours range from  $-0.4$  to  $0.4$  in steps of 0.1. Panel e shows the case  $R_{\text{fold}} > 0$ , while panel f shows the case  $R_{\text{fold}} < 0$ . Recall that folds have  $d_1 \ll d_2 \sim R_{\text{ein}}$ , cusps have  $d_1 \sim d_2 \ll R_{\text{ein}}$ , and crosses have  $d_1 \sim d_2 \sim R_{\text{ein}}$ . The region outside the triangles is inaccessible for this lens potential. Note that the figures were generated with Monte Carlo simulations, and the sampling is imperfect at  $d_1 \sim d_2 \ll R_{\text{ein}}$ .

cation along the fold caustic even when the source is far from a cusp. This point is profound, because the location of the source along the caustic is not observable, and cannot really be determined from the properties of the two images in the fold pair; it can only be inferred by considering the properties of the other two images as well. In particular, the distance

$d_2$  to the next nearest image gives some indication of the location of the source along the caustic, and therefore plays a strong role in the fold relation.

We begin to suspect that using the fold relation in practice is not a simple matter of finding a close pair of images and asking how much they deviate from  $R_{\text{fold}} \approx 0$ ; the fold relation

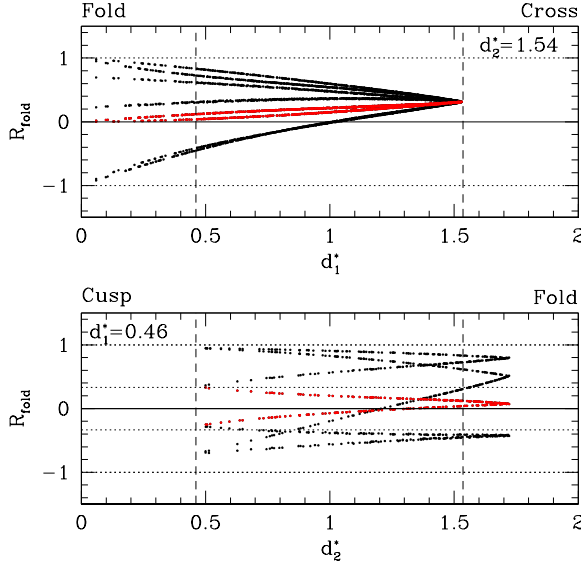


FIG. 4.— (Top)  $R_{\text{fold}}$  as a function of the distance  $d_1^*$ , for fixed  $d_2^* = 1.54$ . Moving from left to right smoothly changes the image configuration from fold to cross. There are multiple curves because there are four image pairs for each image configuration, and there may be two different configurations with the same  $(d_1^*, d_2^*)$ . For each configuration, the smallest-separation pair is marked in red. (Bottom)  $R_{\text{fold}}$  as a function of the distance  $d_2^*$ , for fixed  $d_1^* = 0.46$ . Moving from left to right smoothly changes the image configuration from cusp to fold. The horizontal lines show various asymptotic limits:  $R_{\text{fold}} \rightarrow 0$  for an ideal fold pair;  $R_{\text{fold}} \rightarrow \pm 1/3$  for the two pairs of an ideal cusp triplet; and  $R_{\text{fold}} \rightarrow \pm 1$  for two other pairs in an ideal fold or cusp lens. The vertical lines indicate the separations for our archetypal lenses:  $d_1^{*\text{fold}} = d_1^{*\text{cusp}} = d_2^{*\text{cusp}} = 0.46$ , and  $d_2^{*\text{cusp}} = d_1^{*\text{cross}} = d_2^{*\text{cross}} = 1.54$ . We use an isothermal ellipsoid lens with ellipticity  $e = 0.5$ , and quote all lengths in units of  $R_{\text{ein}}$ .

is in truth more subtle and rich.

#### 4.3. For all four image pairs

So far, among the four images in a given configuration we have only examined the pair with the smallest separation, because the fold relation best describes close pairs. The formalism can be applied to any pair, however, and to round out our general understanding of the fold relation it is instructive to examine all the pairs.

Figure 4 shows  $R_{\text{fold}}$  for all minimum/saddle image pairs, as a function of the distances  $d_1^*$  and  $d_2^*$  that characterize the image configuration. In the top panel we fix  $d_2^*$ , so varying  $d_1^*$  morphs the configurations from folds to crosses. The largest value of  $d_1^*$  corresponds to a symmetric cross, in which case the two minima are identical and the two saddles are identical, so all four minimum/saddle pairs have the same value of  $R_{\text{fold}}$ . In the limit  $d_1^* \rightarrow 0$  we obtain ideal folds, and the fold pair converges to  $R_{\text{fold}} \rightarrow 0$  (the ideal fold relation). In this limit two other pairs converge to  $R_{\text{fold}} \rightarrow \pm 1$ , which is easily understood: the two fold images (A and B in Fig. 1) have much higher magnifications than the two other images, so the pairs AD and CB will both have  $R_{\text{fold}} \rightarrow \pm 1$ . There is no intuitively obvious asymptotic limit for the pair of non-fold images (CD). The figure suggests that such limits do exist, but we suspect that they depend on properties of the lens potential in ways that the limits  $R_{\text{fold}} \rightarrow 0$  and  $\pm 1$  do not.

In the bottom panel we fix  $d_1^*$ , so varying  $d_2^*$  morphs the configurations between folds and cusps. Here the fold limit does not quite reach  $R_{\text{fold}} \rightarrow 0$  and  $\pm 1$  because we have fixed  $d_1^*$  to a finite value that does not actually correspond to an

ideal fold. The more interesting limits are in the direction of cusps. As  $d_2^* \rightarrow d_1^*$  we obtain a symmetric cusp configuration. For a symmetric ideal cusp, we can predict  $R_{\text{fold}} \rightarrow \pm 1/3$  and  $\pm 1$  based on the following logic. By symmetry,  $F_A = F_C$  so the ideal cusp relation implies  $F_B \approx 2F_A$ , and the fold relation then yields  $R_{\text{fold}} \approx \pm 1/3$ . The sign is + for a long-axis cusp (in which case B is a saddle), or - for a short-axis cusp (B is a minimum). At the same time, in an ideal cusp the images A, B, and C are all much brighter than the fourth image D, so any pair involving D has  $R_{\text{fold}} \approx \pm 1$ . Our archetypal cusp lens does not quite reach these asymptotes because the source lies a finite distance from the cusp ( $d_1^*$  is 0.46 rather than  $\approx 0$ ), but it does confirm the basic reasoning.

Examining  $R_{\text{fold}}$  for widely-separated image pairs in this way does not really tell us about small-scale structure, because we are no longer restricted to short length scales. Nevertheless, it is still helpful for obtaining a general understanding of the fold relation.

#### 5. THE FOLD RELATION IN REALISTIC LENS POTENTIALS

While the ideal fold relation  $R_{\text{fold}} \approx 0$  is completely general, it is only valid when the source is extremely close to a caustic. In realistic situations, the better approximation  $R_{\text{fold}} = A_{\text{fold}} d_1$  depends on the source position and properties of the lens potential. In Paper I, we explicitly showed that the properties of the lens potential affecting the cusp relation are ellipticity, low-order multipole modes, and tidal shear. Here, we simply *define* a “realistic smooth lens” to be one that has these angular structures. (See §1 for more discussion.) Unfortunately, the ellipticity, multipole moments, and shear in individual lenses cannot be observed directly. Ellipticity and multipole modes in the lens galaxy *light* may be measurable, but for lensing we need the properties of the *mass*. The mass properties could be constrained with lens modeling (with perhaps the best example being the analysis by Yoo et al. 2005), but we seek to avoid model dependence as much as possible. Instead, our approach is to adopt observationally motivated priors on the distribution of ellipticity, multipole modes, and shear and use Monte Carlo simulations to derive probability distributions for  $R_{\text{fold}}$  for a realistic lens population.

##### 5.1. Methods

The simulation methods are the same as in Paper I, so we review the main points here and refer the reader to that paper for further details. We consider only isothermal radial profiles ( $\Sigma \propto R^{-1}$ ) for the simulated galaxies, because in Paper I we showed that local analyses of the lens mapping are not very sensitive to changes in the radial profile. For the angular structure, we consider ellipticity as well as additional octopole modes ( $m = 4$  multipole perturbations). To model populations of early-type galaxies, we draw the ellipticities and octopole moments from measurements of isophote shapes in observed samples of early-type galaxies. Even if the shapes of the light and mass distributions are not identical on a case-by-case basis, it seems reasonable to think that their distributions may be similar (see Rusin & Tegmark 2001). Indeed, the distribution of isodensity contour shapes in simulated merger remnants is very similar to the observed distribution of isophote shapes (Heyl et al. 1994; Naab & Burkert 2003). We use three different observational samples, because they have different strengths and weaknesses and allow a check for systematic effects:

- Jørgensen, Franx, & Kjærgaard (1995) report ellipticities for 379 E/S0 galaxies in 11 clusters, including

Coma. Their ellipticity distribution has mean  $\bar{e} = 0.31$  and dispersion  $\sigma_e = 0.18$ .

- Bender et al. (1989) report ellipticities and octopole moments for 87 nearby, bright elliptical galaxies. Their ellipticity distribution has mean  $\bar{e} = 0.28$  and dispersion  $\sigma_e = 0.15$ , while their octopole moment distribution has mean  $\bar{a}_4 = 0.003$  and dispersion  $\sigma_{a_4} = 0.011$ .
- Saglia, Bender, & Dressler (1993) report ellipticities and octopole moments for 54 ellipticals in Coma. Their ellipticity distribution has  $\bar{e} = 0.30$  and  $\sigma_e = 0.16$ , while their octopole moment distribution has  $\bar{a}_4 = 0.014$  and  $\sigma_{a_4} = 0.015$ .

The ellipticity and octopole distributions for the three samples are shown in Fig. 6 of Paper I.

For the external shear amplitude, we adopt a lognormal distribution with median  $\gamma = 0.05$  and dispersion  $\sigma_\gamma = 0.2$  dex. This is consistent with the distribution of shears expected from the environments of early-type galaxies, as estimated from  $N$ -body and semianalytic simulations of galaxy formation by Holder & Schechter (2003). It is broadly consistent with the distribution of shears required to fit observed lenses. Dalal & Watson (2004) use a halo model calculation to suggest that the median shear should be more like  $\gamma = 0.03$ . However, the smaller median shear is not very compatible with the shears required to fit observed four-image lenses (e.g., Keeton et al. 1997). Furthermore, if we want to determine how much  $R_{\text{fold}}$  can deviate from zero for smooth lens potentials, then the conservative approach is to adopt the larger median shear. We assume random shear directions.

For each combination of ellipticity, octopole moment, and shear<sup>10</sup> we choose random sources with density  $\sim 10^3 R_{\text{ein}}^{-2}$ , solve the lens equation using the software by Keeton (2001), and compute  $(d_1, d_2, R_{\text{fold}})$  for each minimum/saddle image pair. For each input distribution, we examine a total of  $\sim 10^6$  mock four-image lenses. Note that choosing sources with uniform density in the source plane has two important consequences. First, it ensures that each lens potential is *automatically* weighted by the correct lensing cross section. Second, it means that we neglect magnification bias, which would favor lenses with higher amplifications, and therefore give more weight to sources near the caustics that produce *small* deviations from the ideal fold relation. We therefore believe that neglecting magnification bias is the conservative approach when seeking to understand how large the deviations can be for smooth lens potentials.

## 5.2. First results

We use our ensemble of mock image configurations to extract the probability distribution for  $R_{\text{fold}}$  at fixed values of  $d_1$  and  $d_2$ .<sup>11</sup> Conceptually, this is like going to the appropriate point in the  $(d_1, d_2)$  plane of Figure 3e-f and reading off  $R_{\text{fold}}$ , except that we now consider a large ensemble of lens potentials. To illustrate how we use these distributions, Figure 5 compares the value of  $R_{\text{fold}}$  for each image pair in our archetypal fold, cusp, and cross lenses to the appropriate conditional probability distribution  $p(R_{\text{fold}}|d_1, d_2)$  derived

<sup>10</sup> Note that we need not specify the galaxy mass, because for an isothermal lens the mass merely sets the length scale  $R_{\text{ein}}$ , and we can always work in units such that  $R_{\text{ein}} = 1$ .

<sup>11</sup> Strictly speaking, to accommodate our finite sampling of phase space, we consider all image configurations within  $\pm 0.05$  of the specified  $d_1$  and  $d_2$  values.

from the Monte Carlo simulations. If the observed value lies outside the predicted distribution, then we conclude that the image pair is inconsistent with lensing by a realistic population of smooth lens potentials. It is reassuring to see that our archetypal lenses — which were generated with a smooth lens — are indeed found to be consistent with lensing by a smooth potential.

We can observe some of the general features identified in §4.3. Many of the distributions are bimodal, and some of those have two completely disjoint peaks. This is because given values of  $d_1$  and  $d_2$  can correspond to multiple source positions that yield different  $R_{\text{fold}}$  values (see Fig. 3). In the fold lens, the pair involving two fold images (AB) has  $R_{\text{fold}} \approx 0$ . The two pairs involving one fold and one non-fold image (CB and AD) each have  $|R_{\text{fold}}|$  large; they do not have  $R_{\text{fold}} \rightarrow \pm 1$  because the source sits a finite distance from the caustic, but the general trend that the fold pair has small  $|R_{\text{fold}}|$  while the two fold/non-fold pairs have large  $|R_{\text{fold}}|$  is confirmed. In the cusp lens, two pairs have  $R_{\text{fold}} \approx \pm 1/3$  while the other two have  $|R_{\text{fold}}|$  large. Again, the reason that the peaks in the AD and CD pairs do not actually reach  $R_{\text{fold}} \rightarrow \pm 1$  is because the source sits a finite distance from the caustic. Finally, in the cross case all four pairs have similar  $R_{\text{fold}}$  distributions — identical in the case of a symmetric cross — which are centered at some positive value but fairly broad. The consistency between our general analytic arguments and our detailed Monte Carlo simulations is reassuring, and indicates that we have obtained new, deep insights into the fold relation.

## 6. APPLICATION TO OBSERVED LENSES

We are finally ready to examine the fold relation for observed four-image lenses. We summarize the data here (§6.1), and provide more details in Appendix B. Our main interest for the fold relation is of course fold image pairs (§6.2), but it is still interesting to consider the other image pairs in fold lenses (§6.3), as well as image pairs in cusp (§6.4) and cross (§6.5) lenses.

### 6.1. Summary of the data

Table 1 lists the values of  $d_1$ ,  $d_2$ ,  $R_{\text{ein}}$ , and  $R_{\text{fold}}$  for all minimum/saddle image pairs in 22 known four-image lens systems,<sup>12</sup> and Appendix B provides some comments about the data. Most available flux ratio data come from broad-band optical/near-infrared images or radio continuum observations. We consider separate optical and radio  $R_{\text{fold}}$  values, since they correspond to very different source sizes and therefore provide different information about small-scale structure. We also consider any other flux ratio data that are available: for the mid-infrared for Q2237+0305 (Agol et al. 2000), and the optical broad emission lines for HE 0435–1223 (Wisotzki et al. 2003) and WFI 2033–4723 (Morgan et al. 2004a).

We need the Einstein radius  $R_{\text{ein}}$  to normalize  $d_1$  and  $d_2$ . This must be determined from lens models, but it is quite robust and not very dependent on the choice of model (e.g., Kochanek 1991; Cohn et al. 2001). In the model we use, the main lens galaxy is treated as an isothermal ellipsoid with surface mass density

$$\kappa(r, \theta) = \frac{\Sigma(r, \theta)}{\Sigma_{\text{crit}}} = \frac{R_{\text{ein}}}{2r[1 - \epsilon \cos 2(\theta - \theta_e)]^{1/2}}, \quad (4)$$

where  $\Sigma_{\text{crit}}$  is the critical surface density for lensing,  $\epsilon$  is related to the axis ratio  $q$  of the galaxy by  $\epsilon = (1 - q^2)/(1 + q^2)$ ,

<sup>12</sup> We do not analyze 0047–2808, as discussed in Appendix B.

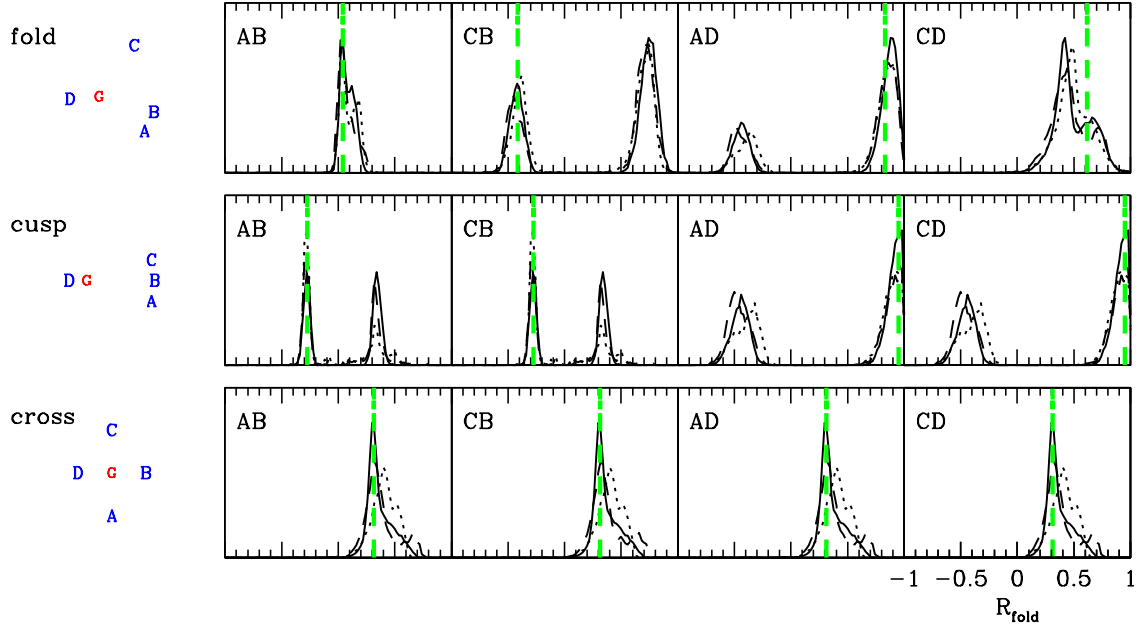


FIG. 5.— Probability distributions for  $R_{\text{fold}}$ . On the left we show the image configurations, with lensed images (A–D) marked in blue and the lens galaxy (G) marked in red. The four columns then show  $R_{\text{fold}}$  for the different image pairs, sorted by increasing  $d_1$  from left to right. (We adopt the convention of naming each pair such that the first letter indicates the minimum image while the second letter indicates the saddle.) The green vertical lines mark the actual values for our archetypal lenses. The black curves show the predicted distributions for realistic lens populations, with solid, dashed, and dotted curves showing results for Monte Carlo simulations based on the Jørgensen, Bender, or Saglia galaxy samples, respectively. The predicted distributions are normalized to unit area.

and  $\theta_e$  is the position angle of the galaxy. Few four-image lenses can be fit by a pure isothermal ellipsoid model, because elliptical lens galaxies tend not to be isolated. In most cases, modeling the environmental contribution to the lens potential as an external shear provides an excellent fit to the image positions (e.g., Keeton et al. 1997). The only exceptions are HE 0230–2130, MG J0414+0534, RX J0911+0551, and B1608+656, each of which is known to have a satellite galaxy near the main lens galaxy that must be included in order to fit the image positions (Wisotzki et al. 1999; Schechter & Moore 1993; Koopmans et al. 2003b). We treat the satellite galaxies as isothermal spheres. We stress that when fitting the models to determine  $R_{\text{ein}}$ , we use only the relative positions of the images and the lens galaxy as constraints; it is not necessary to use the flux ratios as model constraints.

Figure 6 shows how the observed lenses populate the  $(d_1, d_2)$  plane. Although we have labeled them as folds, cusps, and crosses, in fact there is no sharp distinction between the fold and cross samples. SDSS 0924+0219 and B1933+503, which have  $d_1/R_{\text{ein}} \sim 0.9$ , could arguably be relabeled as crosses, although we choose not to do so (see §6.2). The smooth transition simply reflects the fact that there are no sharp boundaries between different four-image configurations in the source plane.

In the figure there is a particular region occupied by simulated lenses (the grayscale), but it is specific to an isothermal ellipsoid lens with ellipticity  $e = 0.5$ . Varying the ellipticity and/or adding shear would move the upper edge so that the region could accommodate the other cross lenses. The two fold lenses at  $d_2/R_{\text{ein}} \sim 2$  are a different story, though. These are HE 0230–2130 and B1608+656, each of which has two lens galaxies. Turning this around, we may say that observed lenses that are outliers in the  $(d_1, d_2)$  plane are likely to have complex lens potentials containing multiple galaxies.

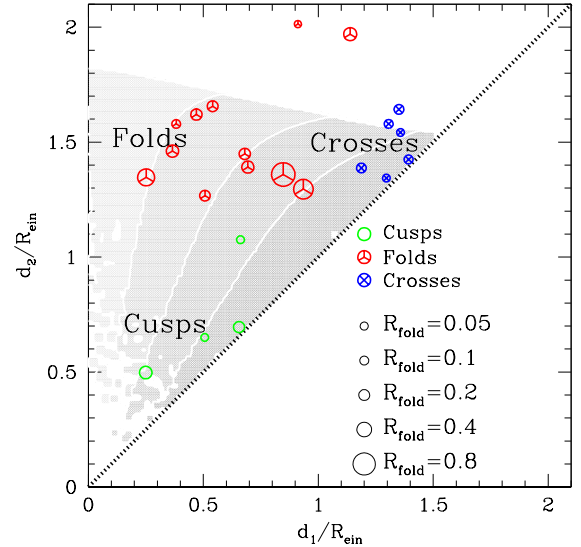


FIG. 6.— Colored points mark the locations of known four-image lenses in the plane of  $d_1/R_{\text{ein}}$  and  $d_2/R_{\text{ein}}$ . The color indicates the visual classification as a fold, cusp, or cross, while the point size indicates the value of  $R_{\text{fold}}$ . To help guide the eye, the grayscale shows  $R_{\text{fold}}$  for an isothermal ellipsoid lens with ellipticity  $e = 0.5$  (from Fig. 3e).

## 6.2. Fold image pairs

We now examine the fold relation by comparing the observed  $R_{\text{fold}}$  values to the distributions expected for a realistic galaxy population. Figures 7–8 show the comparisons for the 12 fold lenses, arranged in order of increasing  $d_1^*/R_{\text{ein}}$ .<sup>13</sup>

<sup>13</sup> Note that we now include B0712+472 among the folds, even though we considered it a cusp in Paper I. Both classifications seem valid, depending on

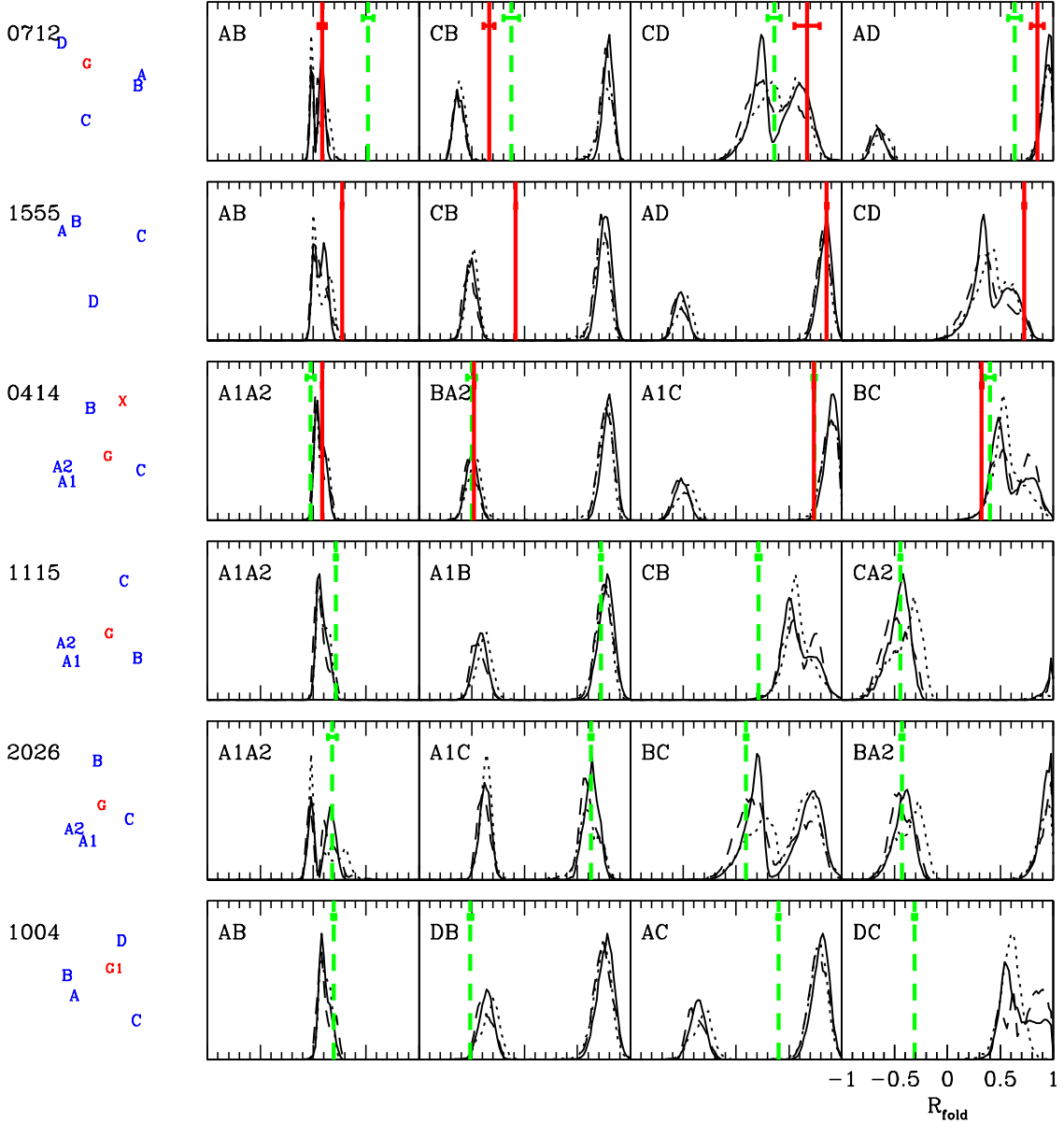


FIG. 7.— Observed and predicted  $R_{\text{fold}}$  values, for six of the known fold lenses. The black curves show the predicted distributions for realistic lens populations, as in Fig. 5. The vertical colored lines show the observed values and their uncertainties, with green indicating optical/near-infrared data and red indicating radio data. (The data are given in Table 1.) The lenses are sorted by increasing  $d_1^*/R_{\text{ein}}$  from top to bottom. For each lens, the image pairs are sorted by increasing  $d_1/R_{\text{ein}}$  from left to right.

While there is a tremendous amount of information here, the discussion in §4 helps us pick out the main trends. First let us consider the various predicted distributions. When  $d_1^*/R_{\text{ein}}$  is small,  $R_{\text{fold}}$  for the fold pair (Column 1) is predicted to lie in a very narrow range near zero. This is the fold relation in its familiar form. At the same time, two other image pairs have distributions that feature two narrow and well-separated peaks (compare the top row of Fig. 5), while the fourth pair has a broad distribution with no particular center. As  $d_1^*/R_{\text{ein}}$  increases, the distribution for the fold pair broadens while the two peaks for the next closest pair (Column 2) tend to move closer together. HE 0230–2130 and B1608+656 buck

one’s purpose. The close pair AB can be considered a fold, while the close triplet ABC can be considered a cusp. The source must lie close to the caustic in a region not far from a cusp. For the purposes of this paper, it is a fold.

these trends, for a simple reason: they have two lens galaxies, so they have configurations that are rare in our Monte Carlo simulations,<sup>14</sup> and that leads to narrow and unusual predicted  $R_{\text{fold}}$  distributions.

For most image pairs, there are no tremendous differences between the  $R_{\text{fold}}$  distributions from the three different simulations (based on the Jørgensen, Bender, or Saglia galaxy samples). This gives us confidence that our conclusions are robust in the sense of not being very sensitive to the choice of input data.

Now we turn to the observed values of  $R_{\text{fold}}$ . Many of them

<sup>14</sup> In fact, the Jørgensen and Saglia simulations do not contain *any* configurations with the same  $d_1$  and  $d_2$  values as the BD pair in B1608+656, to within the sampling resolution of our Monte Carlo simulations.

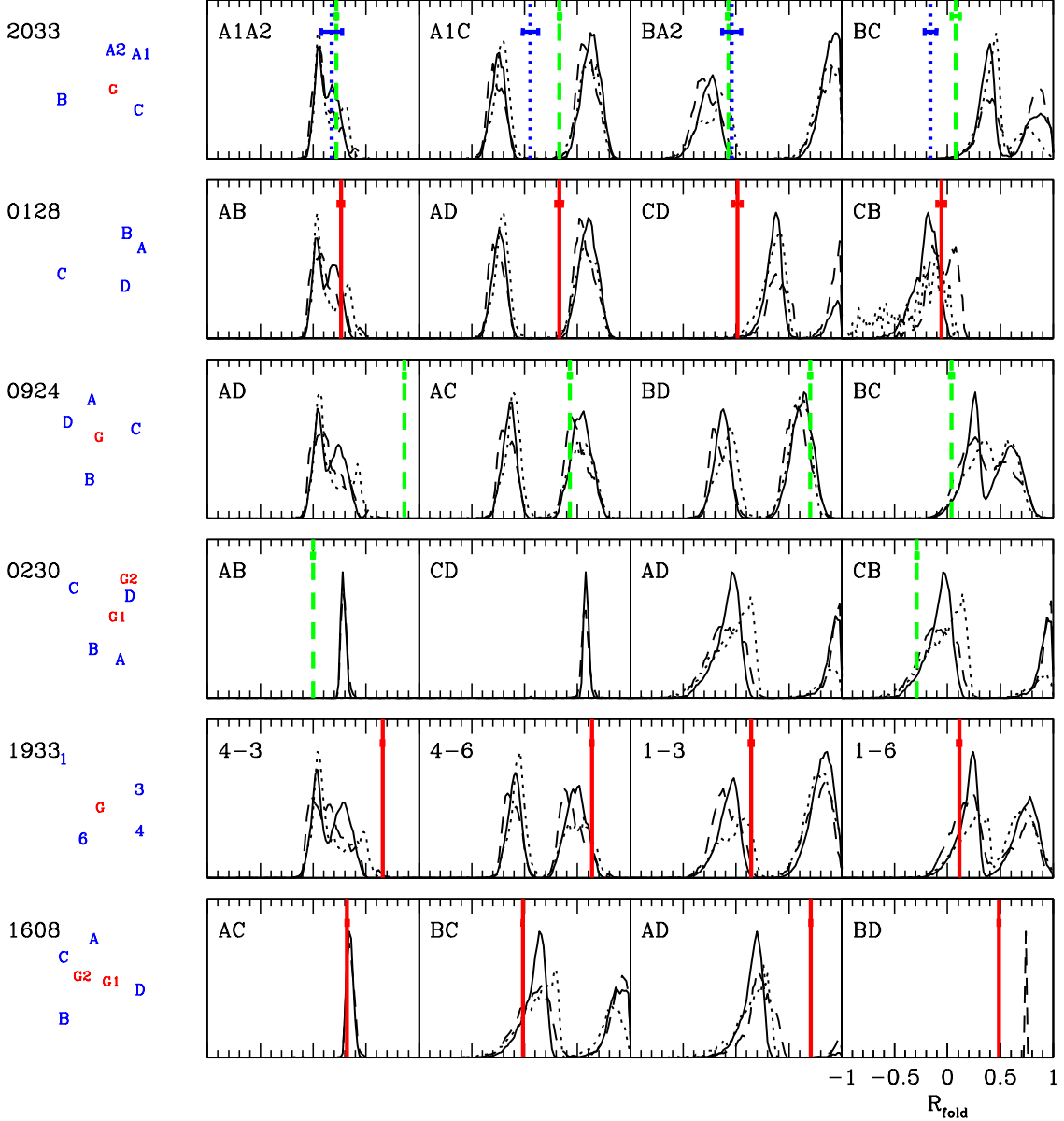


FIG. 8.— Similar to Fig. 7, but for the remaining six known fold lenses (again sorted by  $d_1^*/R_{\text{ein}}$ ). For WFI 2033–4723, the vertical green lines show data from broad-band optical flux ratios, while the vertical blue lines show data from optical emission line flux ratios (Morgan et al. 2004a).

lie within the predicted range, so there is no obvious violation of the fold relation. The outliers are as follows:

**B0712+472:** The optical data grossly violate the fold relation, but the radio data do not. This is consistent with Paper I, in which we found that the optical data strongly violate the cusp relation, while the radio data are marginally different from the predictions. The wavelength dependence suggests that the cause of the optical anomaly may be microlensing.

**B1555+375:** The radio data violate the fold relation at high confidence. To see this more clearly, Figure 9 shows a close-up of the results for the AB image pair. Here we can see typical differences between the predicted distributions for the three simulations, but those differences do not affect our conclusions. The cumulative probability distributions show that the data violate the fold relation at more than 99.6% confidence for all three simulations.

**PG 1115+080:** The optical value of  $R_{\text{fold}}$  differs from the predictions at 99.2% confidence for the distributions based on the Jørgensen and Saglia data, but only 96.1% confidence for the distribution based on the Bender data. Apparently the distribution of octopole moments in the Bender galaxies can help explain the observed  $R_{\text{fold}}$  value, at least enough to reduce the violation of the fold relation from strong to marginal. With detailed lens modeling, Kochanek & Dalal (2004) likewise found that octopole modes make it possible to fit the observed flux ratios, but asserted that the required amplitudes are unphysically large. Yoo et al. (2005) then showed that large multipole modes are inconsistent with the Einstein ring image of the quasar host galaxy. In other words, it does appear that the flux ratio is anomalous. However, we find that the model-independent evidence for the anomaly in PG 1115+080 is not quite as secure as for the other fold anomalies.

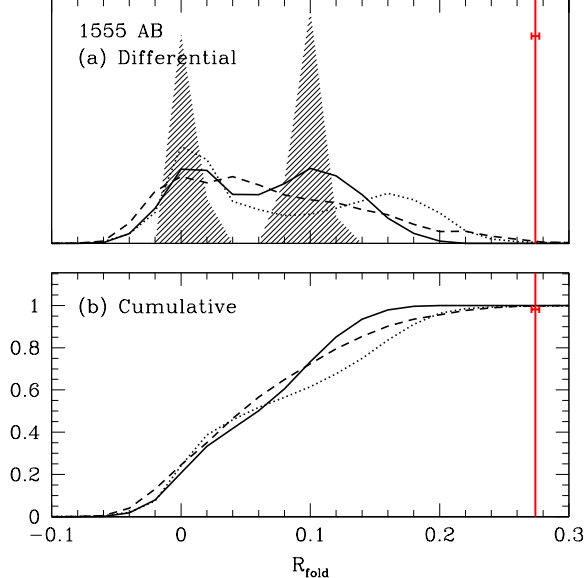


FIG. 9.— (a) Close-up of the AB panel for B1555+375 from Fig. 7. The red line shows the observed radio value for  $R_{\text{fold}}$ , with its uncertainty (see Table 1). The solid, dashed, and dotted curves show the predicted  $R_{\text{fold}}$  distributions for Monte Carlo simulations based on the Jørgensen, Bender, and Saglia galaxy samples, respectively. For comparison, the hatched region shows the distributions for an isothermal ellipsoid with ellipticity  $e = 0.5$ . (b) Similar to panel a, but showing cumulative probability distributions.

**SDSS 0924+0219:** Even though AD is not a particularly close pair (causing the predicted  $R_{\text{fold}}$  distribution to be fairly broad), image D is so faint that there is a gross violation of the fold relation in the optical data. This is similar to our conclusion in Paper I that the flux ratios violate the cusp relation as well.

**HE 0230–2130:** Curiously, the optical value  $R_{\text{fold}} = 0.000 \pm 0.008$  indicates that A and B are *more similar* than expected. This discrepancy is presumably explained by presence of a second lens galaxy, which is not accounted for in our simulations of smooth lens potentials. In other words, it is associated with complex but not small-scale structure in the lens potential. This does raise the question of whether any of the other flux ratio anomalies could be caused by something rather large like a second galaxy, as opposed to small-scale structure. We should stress that in HE 0230–2130 the second galaxy was already known from direct observations as well as analyses of the image positions (see §6.1). Similarly, a second galaxy is known to be present in B1608+656. These examples indicate that it is difficult for a massive second galaxy to escape detection by one means or another, and suggest that the “second galaxy” hypothesis is probably not a valid explanation for most flux ratio anomalies.

**B1933+503:** Although the 4/3 image pair is not particularly close, image 4 is so bright that there is a violation of the fold relation in the radio data at more than 99.6% confidence.

**B1608+656:** This case is interesting because the lens potential is known to contain two lens galaxies. The agreement between the observed  $R_{\text{fold}}$  value and the distribution predicted for smooth lens potentials seems coincidental.

To summarize, our analysis of the fold relation reveals two flux ratio anomalies that were already known from violations of the cusp relation (B0712+472 optical, and SDSS 0924+0219 optical). It also reveals strong new evidence for fold flux ratio anomalies in B1555+375 (radio) and

B1933+503 (radio), plus good but slightly less strong evidence for a fold anomaly in PG 1115+080 (optical). In addition, a violation of the fold relation in HE 0230–2130 (optical) is presumably due to the presence of a second lens galaxy in that system.

While these specific conclusions are valuable, there are some important general lessons as well. First, even the closest observed image pairs have predicted  $R_{\text{fold}}$  distributions with a finite width. Therefore, a non-zero  $R_{\text{fold}}$  value in the range  $R_{\text{fold}} \sim 0–0.2$  *cannot* generally be taken to indicate a flux ratio anomaly. As a rule of thumb, when  $d_1/R_{\text{ein}} \lesssim 0.4$  it does appear that a value  $R_{\text{fold}} \gtrsim 0.2$  is likely to indicate an anomaly, although we caution that this is just a rule of thumb and a full analysis of the predicted  $R_{\text{fold}}$  distribution must be done to reliably identify an anomaly.

The importance of the full analysis becomes clear when we consider PG 1115+080, WFI 2026–4536, and SDSS 1004+4112. These three lenses have similar configurations with  $d_1/R_{\text{ein}} \approx 0.5$ , and (curiously enough) they all have  $R_{\text{fold}} \approx 0.2$ . Yet one is anomalous (PG 1115+080), while the other two are fully compatible with the predicted distributions. What’s more, the predicted distributions for WFI 2026–4536 are bimodal and qualitatively different from those for the other two lenses, even though all three image configurations are visually similar. These lenses teach the lesson that identifying fold flux ratio anomalies is not a simple matter of finding a close pair of images and asking whether  $R_{\text{fold}} \approx 0$ . The distance from  $R_{\text{fold}} \approx 0$  that is needed to provide strong evidence for an anomaly depends in a complicated way on various properties of the lens potential that cannot be directly observed. Only a full and careful analysis of the fold relation can handle these issues.

We conclude that violations of the fold relation can be used to find flux ratio anomalies in a fairly model-independent way. However, that analysis is more subtle than was previously realized. It is necessary to know not only the separation  $d_1$  between the two images, but also the distance  $d_2$  to the next nearest image, and to account for the finite width of the  $R_{\text{fold}}$  distribution expected for smooth lenses.

Finally, it is worthwhile to comment that all twelve of the fold image pairs have  $R_{\text{fold}}$  values that are positive or consistent with zero. An important prediction to emerge from theoretical studies is that small-scale structure should tend to amplify minimum images and/or suppress saddle images (Metcalfe & Madau 2001; Schechter & Wambsganss 2002; Keeton 2003; Bradač et al. 2004). Since either possibility would make  $R_{\text{fold}} > 0$ , seeing only non-negative values is certainly consistent with the substructure hypothesis (see Kochanek & Dalal 2004). It is inconsistent with non-gravitational explanations of flux ratio anomalies (such as extinction or scattering), because those should affect minimum and saddle images in the same way. What is less clear is whether lumpy substructure is the only thing that can explain the asymmetry between minima and saddles, or whether small-scale but smooth structure is a viable alternative. Our analysis does offer an intriguing hint: nearly all the weight in our predicted  $R_{\text{fold}}$  distributions lies at  $R_{\text{fold}} > 0$ , which indicates that even smooth, global features like ellipticity and shear affect minima and saddles differently. Still, it is not clear whether smooth features can explain the further asymmetry that all the anomalous  $R_{\text{fold}}$  values *exceed* the predictions. The minimum/saddle asymmetry appears to be a very promising probe of small-scale structure, but much more study is clearly called for.

### 6.3. Other image pairs in fold lenses

We can also consider the  $R_{\text{fold}}$  values for the other image pairs in fold lenses, although we must be careful about how we interpret them. As discussed in §§4.3 and 5.2, there are some useful general properties of the fold relation for these other image pairs; for example, we expect  $|R_{\text{fold}}|$  to be “large” — closer to unity than zero — for a pair comprising a fold image and a non-fold image. In detail, we are not aware of a simple way to predict the expected  $R_{\text{fold}}$  values; but Figures 7–8 suggest that there is a fairly universal distribution at least for the second-closest image pair (Column 2), which depends mainly on  $d_1^*/R_{\text{ein}}$ .

It therefore seems reasonable to conclude that the observed value of  $R_{\text{fold}}$  for the CB pair in B1555+375 is probably inconsistent with smooth lens models. Indeed, Dobler & Keeton (2005) recently examined detailed lens models for this system, using an isothermal radial profile and several different angular structures, and concluded that image C is anomalous. (They also found that there must be a second anomaly in either image A or B, which is consistent with our conclusion that the AB pair is anomalous.) We cannot necessarily conclude, however, that the CB pair reveals “small-scale” structure in the lens. The separation between the two images is large enough that their flux ratio could be affected by more global features like low-order multipole modes whose amplitudes are somewhat larger than typical in the galaxy samples we used. Similar conclusions apply to the CB pair in B0712+472.

The CB pair in PG 1115+080 and the CD pair in B0128+437 both show discrepancies between the observed and predicted  $R_{\text{fold}}$  values. However, in these cases the observed values lie in the tail of the predicted distributions, at around the 1% probability level. It is not immediately obvious whether seeing these two “unusual” values among 88 different image pairs is surprising or not. If the 88 pairs were independent, the binomial distribution would indicate that there is a 16% chance of seeing the two unusual values, which would not be very surprising. The 88 pairs are not all independent, though, and it is not clear how many independent pairs we do have. In the conservative limit that we only consider having 22 independent lenses, there is still a 2% chance of seeing the two unusual values. In other words, we cannot rule out the possibility that these two pairs simple represent statistical fluctuations. Another possibility is that modest changes in the assumed distributions of ellipticity, octopole moment, and shear could raise the tail of the predicted  $R_{\text{fold}}$  distribution enough to make the observed values seem even less unusual.

It is important to stress that these arguments do not apply to pairs like CB in B0712+472 and CB in B1555+375, whose observed  $R_{\text{fold}}$  values lie well outside the predicted distributions. When the data are so far from the tails of the predictions, no reasonable adjustments to the input distributions can shift the predictions enough to match the data, and the likelihood that the observed values are a random fluctuation is exceedingly small. Nor do the arguments apply to fold image pairs. When the images lie close to each other and close to a fold critical curve, the predicted distributions are quite insensitive to details of the assumed ellipticity, octopole moment, and shear distributions.

Another interesting set of discrepancies is the AC and DC pairs in SDSS 1004+4112. This lens is produced by a cluster of galaxies (Oguri et al. 2004), so it has a complex lens potential that is certainly not well modeled as an isothermal halo with ellipticity, octopole moment, and shear. The discrepan-

cies between the observed  $R_{\text{fold}}$  values and our predicted distributions is therefore not surprising. Likewise for the A1C and BC pairs in WFI 2033–4723.<sup>15</sup> This lens has one galaxy (called G1) lying just 4'' from the main lens galaxy, and at least five others within 20''. Detailed lens models, treating G1 explicitly and approximating the other galaxies with an external shear, can yield magnification ratios that agree fairly well with the observed values (Morgan et al. 2004a). In other words, the observed  $R_{\text{fold}}$  values in WFI 2033–4723 are indeed inconsistent with lensing by a simple lens potential, and they indicate complex but not necessarily small-scale structure.

This is our general conclusion as well: discrepancies between observed and predicted  $R_{\text{fold}}$  values for the “other” pairs in fold lenses indicate complex structure in the lens potential. It is not necessarily small-scale structure, but it still interesting and worth studying with detailed lens models.

### 6.4. Cusp lenses

A cusp configuration has a close triplet of images that can be thought of as two close pairs. Although all three images lie near a fold critical curve, the two pairs do not satisfy the ideal fold relation  $R_{\text{fold}} \approx 0$  because the analysis leading to that relation breaks down near a cusp critical point. Nevertheless, we saw in §4.3 that we generically expect  $|R_{\text{fold}}| \approx 1/3$  for the two pairs in a symmetric, ideal cusp configuration. The numerical value may change as the source moves around, but we should consider whether the prediction of a bimodal  $R_{\text{fold}}$  distribution with two narrow and well-separated peaks is generic. In other words, we want to see if there is some sort of “fold relation” for cusp lenses, and if it can be used to uncover flux ratio anomalies in these systems.

Figure 10 compares the observed and predicted  $R_{\text{fold}}$  distributions for the four observed cusp lenses. At first glance, it does appear that the two pairs composed of cusp images are predicted to have narrow, bimodal  $R_{\text{fold}}$  distributions. Image pairs like CB in B2045+265 and BA in RX J0911+0551, which have observed  $R_{\text{fold}}$  values lying between and far from the two peaks would therefore seem to indicate anomalies. (These two lenses were both identified as anomalous by the cusp relation; see Paper I.) Closer inspection reveals, however, that this conclusion can be sensitive to the presence or absence of octopole modes, as we can see by examining individual lenses as follows.

**B2045+265:** Consider the CB pair. Our simulations using the Jørgensen galaxy sample (with no octopole modes) predict an  $R_{\text{fold}}$  distribution with two narrow peaks far from the observed radio and optical values. However, our simulations using the Bender and Saglia galaxy samples (both of which include octopole modes) predict that the  $R_{\text{fold}}$  distribution has a tail extending from the upper peak down to  $R_{\text{fold}} \approx 0$  and nearly all the way to the lower peak. To be more specific, without octopole modes there is essentially no chance that the predicted  $R_{\text{fold}}$  value lies within  $3\sigma$  of the observed value. However, with octopole modes that probability can be as high as 5.3% when we compare the predictions to the optical data, or even 9.5% for the radio data. In other words, the possibility that octopole modes may be present significantly limits our ability to declare that the CB pair violates the fold relation. The conclusions are even weaker for the AB pair.

<sup>15</sup> Note that the differences between the optical continuum flux ratios and the emission line flux ratios in this system are interpreted as evidence for microlensing (see Morgan et al. 2004a).

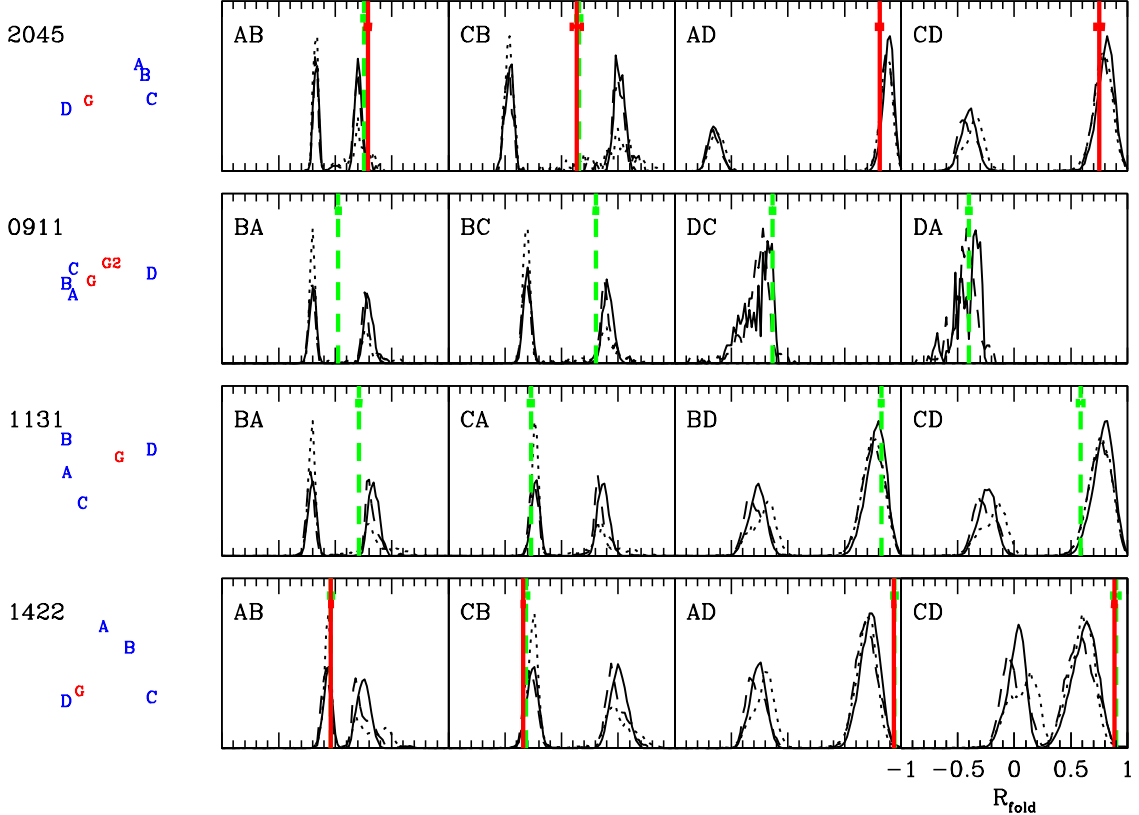


FIG. 10.— Similar to Fig. 7, but for the known cusp lenses. Again, the vertical green lines show optical/near-infrared values of  $R_{\text{fold}}$ , while the vertical red lines show radio values.

These results are surprising for two reasons. First, B2045+265 shows an extremely strong violation of the cusp relation, indicating a significant flux ratio anomaly, but the anomaly is not clearly identified by the fold relation. Second, we found in Paper I that the cusp relation is generally insensitive to octopole modes, while the fold relation (as applied to cusp lenses) is apparently more sensitive. We conjecture that the difference is because the cusp relation considers three images simultaneously, while the fold relation considers them only in two separate pairs.

**RX J0911+0551:** The situation is similar but less dramatic for the BA pair in this lens. The probability that the predicted  $R_{\text{fold}}$  value lies within  $3\sigma$  of the observed optical value is zero when we omit octopole modes, and it rises to at most 0.5% when we allow the modes. This remains a fairly clear violation of the fold relation. For the BC pair, the probability can be as high as 5.2%, so the evidence for a violation of the fold relation is less strong. In one sense these results do not tell us much that is new, because we already knew that this lens has a flux ratio anomaly based on its violation of the cusp relation (see Paper I). However, the fold relation may help us identify which of the three images is most anomalous. Since the violation of the fold relation is stronger in the BA pair than in the BC pair, we might infer that image A is the image most affected by small-scale structure. There could in fact be more than one perturbed image (see Dobler & Keeton 2005 for examples among other lenses), but the fold relation suggests that the strongest anomaly is in image A. The cusp relation was unable to make such a distinction between images.

**RX J1131-1231:** For the BA pair, the probability that the

predicted  $R_{\text{fold}}$  value lies within  $3\sigma$  of the observed optical value is no higher than 2.3%. The corresponding probability for the CA pair can be as high as 46%. This is another lens that is known to have a flux ratio anomaly based on a violation of the cusp relation (Paper I). So again the fold relation does not reveal a new anomaly, but does suggest that the anomaly is probably in image B.

We conclude that there is indeed a fold relation that can be applied to the two pairs of images in a cusp triplet. It appears to be less powerful than the cusp relation for identifying flux ratio anomalies. However, it may help us figure out which of the three images is anomalous.

Finally, we remark that the fold relation does not indicate anomalies among the three cusp images in B1422+231. This is consistent with our conclusion from Paper I, namely that generic magnification relations do not identify anomalies in this lens even though detailed lens modeling suggests that it is indeed anomalous (Mao & Schneider 1998; Bradač et al. 2002; Metcalf & Zhao 2002; Dobler & Keeton 2005). Bradač et al. (2002, 2004) claim that the challenge for smooth lens models is not just the relative brightnesses of images A, B, and C, but also the faintness of image D. This idea is in fact suggested by the fold relation: the observed values of  $R_{\text{fold}}$  for the AD and CD pairs disagree with the predicted distributions at more than 99.6% confidence. However, Dobler & Keeton (2005) were able to find an acceptable model under the hypothesis that only image A is perturbed by small-scale structure. The bottom line is that the nature of the anomaly in B1422+231 is not completely clear, and generic magnification relations are not adequate for fully understanding this

system.

### 6.5. Cross lenses

The image pairs in cross lenses are not close pairs, but for completeness we still consider them in the context of the fold relation. Figure 11 compares the observed and predicted  $R_{\text{fold}}$  values for the six known cross lenses. The predicted distributions are all broad and centered at some positive value of  $R_{\text{fold}}$  (also see Fig. 5 and §5.2). One striking result is that nearly all the weight in the predicted probability distributions lies at  $R_{\text{fold}} > 0$ . In other words, we generally expect minima to be brighter than saddles in cross configurations, at least for our assumed distribution of ellipticities and shears. We return to this point below. Another important result is that the  $R_{\text{fold}}$  distributions predicted by our three simulations do not differ substantially from one another. It appears that the presence or absence of octopole modes does not significantly affect the predictions, perhaps because an  $m = 4$  mode would affect all images in a cross configuration similarly. Finally, when we compare the observed  $R_{\text{fold}}$  values and the predicted distributions, we see the following cases of disagreement.

**Q2237+0305:** Microlensing creates time variability in the optical fluxes (Woźniak et al. 2000) and leads to discrepancies between the data and the predicted distributions; the most obvious example is the BC pair. Of course, it is the time dependence more than the violation of the fold relation that leads to the conclusion that there is small-scale structure in the form of microlensing.

**HE 0435–1223:** In the CB pair, the optical continuum and emission line data ( $R_{\text{fold}} = -0.029 \pm 0.014$  and  $-0.035 \pm 0.010$ ) differ from the predicted distributions at more than 98.7% confidence. However, our detailed ellipsoid+shear lens models for this system fit the data fairly well, yielding a model value  $R_{\text{fold}} = -0.055$ . The reason is that the models are free to set the ellipticity and shear to any values, regardless of whether those values agree with the distributions that go into our Monte Carlo simulations for the general fold relation analysis. The models require an ellipticity  $e = 0.28$  and a shear  $\gamma = 0.13$ . The shear value is  $2\sigma$  above the median for our input distribution, but not unreasonable especially given the complexity of the lens environment (Morgan et al. 2004b). In other words, the discrepancy between the observed  $R_{\text{fold}}$  value and the predicted distributions probably does not reveal small-scale structure, but it does indicate some interesting complexity in the lens potential.

**HST 14176+5226:** The optical values  $R_{\text{fold}} = 0.088 \pm 0.040$  and  $0.164 \pm 0.040$  for the CB and AD pairs (respectively) differ from the predicted distributions at more than 99.3% and 97.7% confidence. In this case, our ellipsoid+shear lens models for this system predict  $R_{\text{fold}} = 0.222$  and  $0.362$  for the two pairs, so they do not agree with the observed values. This lens appears to be inconsistent with lensing by smooth potentials in a way that cannot simply be attributed to the environment. These discrepancies deserve further study.

**HST 14113+5211:** In the CD pair, the optical value  $R_{\text{fold}} = 0.138 \pm 0.049$  differs from the predicted distributions at more than 99.4% confidence. This is another system in which ellipsoid+shear lens models for this system fit the data quite well, yielding a model value  $R_{\text{fold}} = 0.134$ . In this case, the model shear  $\gamma = 0.30$  is very rare in the Monte Carlo simulations, but it is not unreasonable given that the lens is known to lie in a rich cluster of galaxies (Fischer et al. 1998). In other words, this is another system in which the discrepancy between the observed  $R_{\text{fold}}$  value and the predicted distributions indicates

interesting structure in the lens potential that may be associated with the lens environment.

**H1413+117:** The optical value  $R_{\text{fold}} = -0.229 \pm 0.022$  for the DB pair differs from the predicted distributions at more than 99.9% confidence, and is surprising because it is so large and negative. The optical values  $R_{\text{fold}} = -0.056 \pm 0.023$  for the DC pair and  $R_{\text{fold}} = 0.031 \pm 0.016$  for the AB pair differ from the the predicted distributions at more than 99.9% and 99.7% confidence, respectively. This is another system in which ellipsoid+shear lens models can fit (some of) the data fairly well using a large shear. Specifically, with a shear  $\gamma = 0.24$  the model yields  $R_{\text{fold}} = -0.174$  for DB and  $R_{\text{fold}} = -0.026$  for DC. (Note that a large shear can explain the large negative  $R_{\text{fold}}$  value for DB.) The one remaining puzzle is the AB pair: the model yields  $R_{\text{fold}} = 0.141$ , which still disagrees with the observed value. In other words, there appears to be a large shear, and yet the AB pair may still be anomalous, so this system deserves to be studied more carefully.

**HST 12531–2914:** The optical values of  $R_{\text{fold}}$  for the (AC, BC, AD) pairs disagree with the predicted distributions at more than (99.9, 99.8, 97.9) percent confidence, respectively. In particular, both AC and BC have negative values of  $R_{\text{fold}}$ . Detailed lens models show that this is another system that can be fit well by invoking a large shear  $\gamma = 0.28$ . Such a shear is consistent with the general analysis by Witt & Mao (1997) using only image positions to infer the presence of a strong shear. In this case, no source of shear is known yet, but given the compelling evidence for a strong shear, it would be worthwhile to look for complex structure in the lens environment.

This analysis teaches several lessons. Our frequent reference to models for cross lenses indicates that the general fold relation analysis by itself cannot provide a complete understanding of flux ratios in these systems. There are several lenses in which observed  $R_{\text{fold}}$  values disagree with the distributions for our assumed lens population, but agree with reasonable smooth lens models — if the shear is allowed to be large.

A simple example of such discrepancies is found in negative  $R_{\text{fold}}$  values. Our family of smooth lens potentials generally predicts  $R_{\text{fold}} > 0$ , meaning that the two minimum images are brighter than the two saddles. By contrast, several observed lenses have one saddle that is brighter than one or both minima. In Q2237+0305, the bright saddle is caused by microlensing. In several other lenses, we have argued that a bright saddle is associated with a large shear from the lens environment.<sup>16</sup> Finally, in at least two cases (HST 14176+5226, and the AB pair in H1413+117) there are discrepancies that we do not yet understand. The important conceptual result is that bright saddle images (negative  $R_{\text{fold}}$  values) in cross lenses seem to indicate “interesting” structure in the lens potential. That structure may be due to small-scale structure, or the lens environment, or something else; the fold relation cannot tell. But this generic analysis does help us identify lenses that warrant further study.

## 7. CONCLUSIONS

When the source in a four-image gravitational lens system lies sufficiently close to a fold caustic, the two images that straddle the fold critical curve should be mirror images of each other, and the dimensionless flux combination

<sup>16</sup> Since the shear and ellipticity are determined by the image positions, we can be confident that the flux ratio anomalies and discrepancies seen in §§6.2–6.4 are not merely artifacts of large shear. The question remains as to why so many observed cross lenses seem to require large shears.

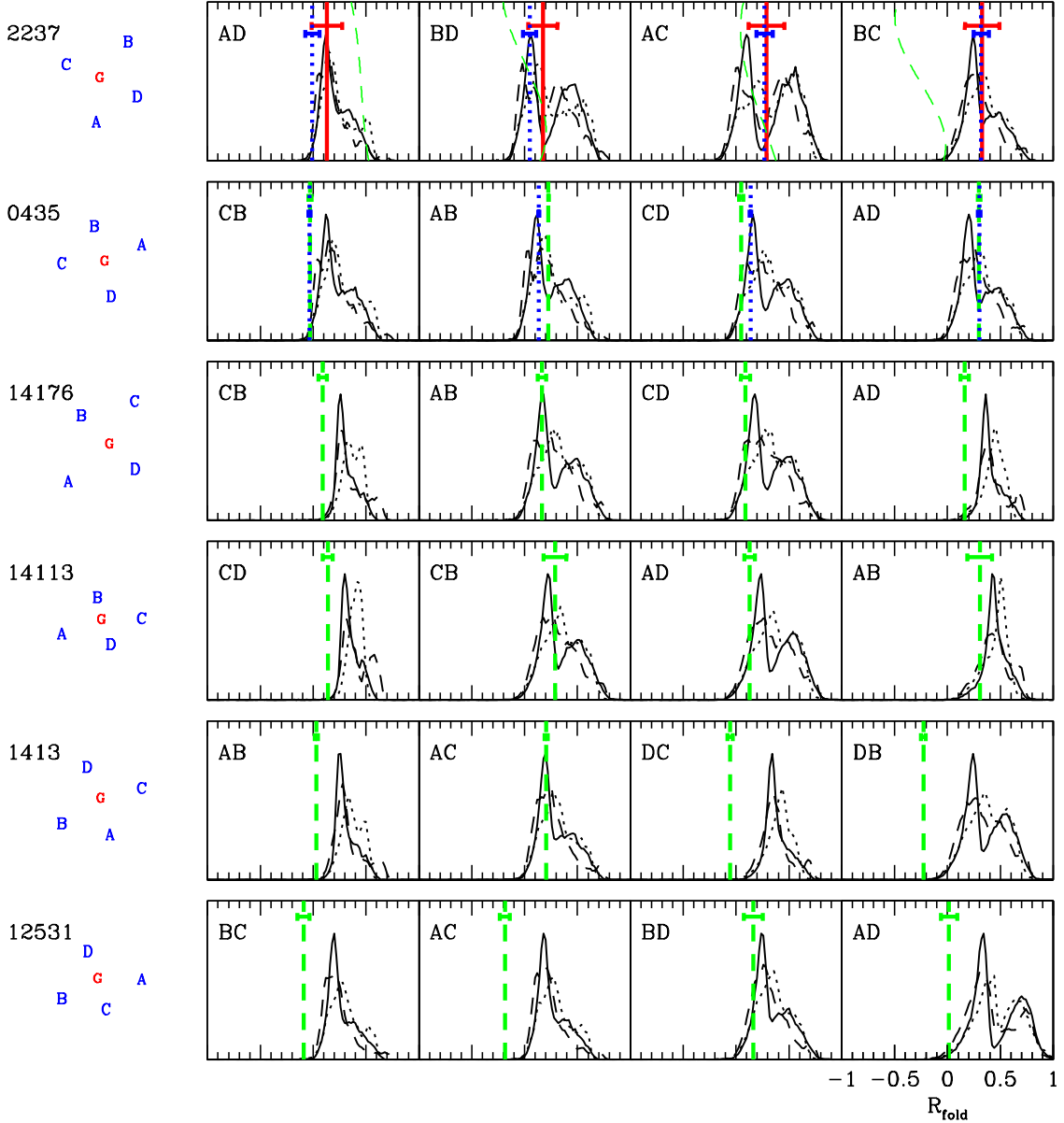


FIG. 11.— Similar to Fig. 7, but for the known cross lenses. For Q2237+0305, the vertical blue lines show mid-infrared values of  $R_{\text{fold}}$  (Agol et al. 2000); also, the green lines bend to represent the time variability in the optical flux ratios (Woźniak et al. 2000), with time running vertically. For HE 0435–1223, the vertical blue lines indicate data from optical emission line flux ratios (Wisotzki et al. 2003).

$R_{\text{fold}} \equiv (F_{\text{min}} - F_{\text{sat}})/(F_{\text{min}} + F_{\text{sat}})$  should vanish. A violation of this “fold relation” in an observed lens is thought to indicate that the lens galaxy has significant structure on scales smaller than the separation between the two close images. The fold relation may therefore join the cusp relation as an important model-independent method for identifying flux ratio anomalies that indicate small-scale structure.

We have learned, though, that the fold relation is more subtle and rich than was previously realized. The ideal fold relation  $R_{\text{fold}} \approx 0$  holds only when the source is asymptotically close to a fold caustic. In more realistic situations, we find  $R_{\text{fold}} \propto u^{1/2} \propto d_1$  where  $u$  is the distance of the source from the caustic, while  $d_1$  is the distance between the two close images. In other words,  $R_{\text{fold}}$  goes to zero fairly slowly as the source approaches the caustic, which means that  $R_{\text{fold}} \neq 0$  might just indicate that the source sits a finite distance from the caustic.

(For comparison, the cusp relation has a more rapid dependence  $R_{\text{cusp}} \propto d^2$ ; see Paper I.) If we seek to use the fold relation to identify flux ratio anomalies that indicate small-scale structure, then we must understand how much  $R_{\text{fold}}$  can deviate from zero because of the finite offset of the source.

This is where we find our most startling result:  $R_{\text{fold}}$  is determined not just by the distance of the source from the caustic, but also by the location of the source *along* the caustic. If we write  $R_{\text{fold}} = A_{\text{fold}} d_1 + \dots$ , then the coefficient  $A_{\text{fold}}$  varies enormously around the caustic. The problem is that the location of the source along the caustic, and hence the value of  $A_{\text{fold}}$ , is not directly observable. Consequently, it is no simple matter to say how large  $R_{\text{fold}}$  must get before we can infer the presence of small-scale structure. Fortunately, the placement of the source along the caustic is encoded in the image configuration: not in the separation  $d_1$  between the close pair of

images, but rather in the distance  $d_2$  to the next nearest image. (For example, a source near a fold but not near a cusp leads to  $d_1 \ll d_2 \sim R_{\text{ein}}$ , while a source near a cusp leads to  $d_1 \sim d_2 \ll R_{\text{ein}}$ .) We may still be able to predict the range of  $R_{\text{fold}}$  possible for a smooth lens potential, but only if we consider  $d_2$  as well as  $d_1$ .

This general understanding allows us to develop a general method for using the fold relation to search for flux ratio anomalies in real lens systems. We postulate a reasonable and realistic population of smooth lens potentials containing ellipticity, octopole modes, and tidal shear, and use Monte Carlo simulations of four-image lenses produced by these lens potentials to derive the conditional probability distribution  $p(R_{\text{fold}}|d_1, d_2)$  for  $R_{\text{fold}}$  at fixed  $d_1$  and  $d_2$  (strictly speaking, fixed  $d_1/R_{\text{ein}}$  and  $d_2/R_{\text{ein}}$ ). We can then compare the observed value of  $R_{\text{fold}}$  for a real lens to the corresponding predicted distribution to determine whether the data are consistent with lensing by a smooth potential. In making our predictions, we actually consider three different galaxy populations in order to understand how our results depend on assumptions about what constitutes a “reasonable and realistic” lens population.

The fold relation applies most directly to the close pair of images in a lens with a fold configuration. Among the 12 known fold lenses, we find evidence for five violations: the optical (but not radio) fluxes in B0712+472; the optical fluxes in SDSS 0924+0219; the optical fluxes in PG 1115+080; the radio fluxes in B1555+375; and the radio fluxes in B1933+503. The optical anomalies in B0712+472 and SDSS 0924+0219 were already known from violations of the cusp relation (see Paper I), but it is valuable to see them identified by the fold relation as well. The optical anomaly in PG 1115+080 is not quite as secure as the others: the confidence level is 99.2% for two of our three sets of predictions, but only 96.1% for one that includes fairly strong octopole modes. Detailed lens modeling of PG 1115+080 suggests that multipole modes cannot provide an acceptable explanation of the flux ratio anomaly (Kochanek & Dalal 2004; Yoo et al. 2005), and while that conclusion is more model-dependent than ours, it does suggest that PG 1115+080 is indeed anomalous. The radio anomalies in B1555+375 and B1933+503 are newly revealed by the fold relation.

We believe that fold flux ratio anomalies provide robust and model-independent evidence for small-scale structure, for two reasons. First, the identification of the anomalies involves a *local* analysis of the lens mapping, and thus relies only on local properties of the lens potential. This is precisely what we want in an analysis aimed at revealing small-scale, local structure. Second, we have explicitly shown that (apart from PG 1115+080) our conclusions do not change if we modify the parameter distributions that define our realistic galaxy population.

Based on our detailed analyses of individual fold lenses, we can extract a few rules of thumb. Since the sources in real lenses always lie a finite distance from a caustic,  $R_{\text{fold}}$  values in the range  $0 \lesssim R_{\text{fold}} \lesssim 0.2$  are predicted to be quite common and probably do *not* indicate flux ratio anomalies. When the separation between the two close images is small ( $d_1/R_{\text{ein}} \lesssim 0.4$ ), the dependence on  $d_2$  is not very strong; all that really matters is having  $d_2$  be large enough for the image configuration to be identified as a fold. In this case, it appears that large values  $R_{\text{fold}} \gtrsim 0.2$  can reveal candidate anomalies. However, the fact that only one of four observed lenses with  $R_{\text{fold}} \approx 0.2$  is anomalous provides a strong reminder that a

full and careful analysis of the fold relation must be done before drawing conclusions about anomalies. Finally, as  $d_1$  increases, so too does the value of  $R_{\text{fold}}$  required to indicate an anomaly, and rules of thumb about the fold relation cease to be valid.

One final rule of thumb is that our smooth lens potentials almost always predict  $R_{\text{fold}} > 0$  for fold image pairs, indicating an asymmetry such that minimum images are generally expected to be brighter than saddle images in fold pairs. This point is probably connected to the prediction that substructure affects minima and saddles differently, tending to amplify minima but suppress saddles (Metcalf & Madau 2001; Schechter & Wambsganss 2002; Keeton 2003; Bradač et al. 2004), and to the observation that anomalous minima seem to be too bright while anomalous saddles seem to be too faint (Kochanek & Dalal 2004; Dobler & Keeton 2005). However, these issues are not yet fully understood, and further study is needed.

Our full understanding of the fold relation also allows us to apply it to the two close image pairs in a cusp lens. This application is more subtle because the analysis underlying the fold relation breaks down near a cusp caustic. Nevertheless, the predicted  $R_{\text{fold}}$  distribution for smooth lenses is bimodal with two narrow and well separated peaks, which constitutes a sort of fold relation that can be used to evaluate observed  $R_{\text{fold}}$  values. We find that applying this fold relation to cusp lenses does not reveal any new anomalies beyond those that were identified by the cusp relation (Paper I). However, it may help us understand which of the three images is anomalous (a distinction that the cusp relation cannot make). For example, it appears that the strongest anomaly in RX J0911+0551 is probably in image A, while the strongest anomaly in RX J1131–1231 is probably in image B. We take these conclusions less as definite statements and more as interesting suggestions to be examined with detailed lens models. One curious qualitative result is that, in cusp lenses, the fold relation appears to be more sensitive than the cusp relation to octopole modes. This fact limits our ability to find a clear violation of the fold relation in B2045+265, even though this lens has a very strong violation of the cusp relation.

Finally, we can also use our full understanding to apply the fold relation to all minimum/saddle pairs in all four images lenses, regardless of how close the pairs are. We must be very careful to remember that when  $d_1 \gtrsim R_{\text{ein}}$  we are no longer performing a *local* analysis of the lens mapping, so we cannot claim to draw any model-independent conclusions about small-scale structure. Nevertheless, it is still interesting to determine which lenses seem to be inconsistent with lensing by an isothermal ellipsoid perturbed by octopole modes and moderate shear. Among fold lenses that do not have fold anomalies, we find that B0128+437, HE 0230–2130, SDSS 1004+4112, and WFI 2033–4723 all have discrepancies between the data and predictions for other image pairs.<sup>17</sup> In three of these cases (SDSS 1004+4112, HE 0230–2130, and WFI 2033–4723), the discrepancies are (presumably) caused by complex structure in the environment of the main lens galaxy. Finally, each of the six known cross lenses has at least one discrepant image pair. In Q2237+0305 the discrepancy is caused by microlensing. In three others (HST 12531–2914, HST 14113+5211, and H1413+117) it may be attributed to

<sup>17</sup> Actually, the discrepancy in HE 0230–2130 is seen in the fold pair, but it can be attributed to the presence of a second lens galaxy so we prefer to discuss it here rather than among the fold flux ratio anomalies.

a large shear from a complex lens environment. Again, we emphasize that discrepancies in the fold relation for large-separation image pairs cannot be taken as strong evidence for small-scale structure. However, they can suggest that the lens potential has some interesting and complex structure that deserves further study.

At this point it is worthwhile to review the lenses in which violations the cusp and fold relations provide model-independent evidence for small-scale structure in the lens potential:

- Among four known cusp lenses, there are three anomalies: RX J0911+0551 (optical), RX J1131–1231 (optical), and B2045+265 (radio).
- Among 12 known fold lenses, there are five anomalies: B0712+472 (optical but not radio), SDSS 0924+0219 (optical), PG 1115+080 (optical), B1555+375 (radio), and B1933+503 (radio).

There may be other anomalies that are not identified by a generic analysis, but that are revealed by detailed lens modeling; B1422+231 is a prime example (Mao & Schneider 1998; Bradač et al. 2002; Metcalf & Zhao 2002; Dobler & Keeton 2005). Moreover, there may be systems among the “discrepant” lenses mentioned above that in fact contain small-scale structure; a good example is Q2237+0305, whose time variable discrepancies are caused by microlensing (Woźniak et al. 2000). In other words, our accounting represents a strict *lower* bound on the number of lenses with flux ratio anomalies caused by small-scale structure — and makes it eminently clear that such anomalies are quite common.

Interpreting these anomalies to place constraints on the nature of the implied small-scale structure involves many considerations that are beyond the scope of this paper. No analysis of single-epoch, single-band photometry can determine the scale of the structure required to explain flux ratio anomalies, beyond the idea that it must be smaller than the separation between the images. Time variability (as in Q2237+0305) or differences between optical and radio flux ratios (as in B0712+472) may indicate microlensing, although

even then a much more detailed analysis is required to determine the microlensing scale (e.g., Kochanek 2004, and references therein). Absent such data, it is impossible for any analysis of broad-band photometry in individual lenses to robustly distinguish between microlensing, millilensing, or intermediate-scale phenomenon. All three possibilities are interesting, but they have very different implications for astrophysics.

Fortunately, there are excellent prospects for obtaining additional data that can help distinguish between the different hypotheses. Even apart from time variability, comparisons between optical continuum and broad-band flux ratios can establish the scale of the small-scale structure (Moustakas & Metcalf 2003; Wisotzki et al. 2003; Metcalf et al. 2004; Morgan et al. 2004a; Wayth et al. 2005). Showing that minima and saddle images are affected differently by small-scale structure might also establish the scale (Metcalf & Madau 2001; Schechter & Wambsganss 2002; Keeton 2003; Kochanek & Dalal 2004; Bradač et al. 2004). These are several examples of the more general point that the size of the source quasar provides a scale in the problem that may help us determine the scale of structure in the lens (Dobler & Keeton 2005). It is important to note that all of these approaches require significant effort to obtain, analyze, and interpret new data; studying *all* four-image lenses in this much detail is not feasible. It is therefore crucial to have a reliable way to identify lenses that warrant further study. The fold relation joins the cusp relation in providing precisely the realistic but robust method that we need for identifying flux ratio anomalies. As such, the two relations provide the foundation for studies of small-scale structure in lens galaxies.

We thank Art Congdon and Greg Dobler for helpful discussions. BSG was supported by a Menzel Fellowship from the Harvard College Observatory. AOP was supported by NSF grants DMS-0302812, AST-0434277, and AST-0433809, and an MIT Martin Luther King, Jr. Visiting Professorship in Physics.

## APPENDIX

### A. UNIVERSAL RELATIONS FOR FOLDS

The generic properties of lensing near a fold caustic have been studied before by Schneider et al. (1992, Chapter 6), Petters et al. (2001, Chapter 9), and Gaudi & Petters (2002a). In this appendix we extend the analysis to a higher order of approximation.

#### A.1. Local orthogonal coordinates

Consider the lens equation  $\vec{y} = \vec{x} - \text{grad } \psi(\vec{x})$ . If we assume that the induced lensing map,  $\vec{\eta}(\vec{x}) = \vec{x} - \text{grad } \psi(\vec{x})$ , from the lens plane to the light source plane is locally stable, then the caustics of  $\vec{\eta}$  must be either folds or cusps (Petters et al. 2001, p. 294). Let us focus on a fold caustic, and translate coordinates in the lens and light source planes so that the caustic passes through the origin  $\vec{y} = 0$  of the light source plane, while the origin  $\vec{x} = 0$  of the lens plane maps into the origin of the light source plane. By abuse of notation, we still use  $\vec{x}$  and  $\vec{y}$  to denote the translated coordinates.

Consider a small neighborhood  $N_L$  about the origin in the lens plane, which maps to a local region  $N_S$  about the origin in the source plane. We assume  $N_S$  is sufficiently small that no critical points outside  $N_L$  are mapped into  $N_S$ , and there are no cusp caustic points inside  $N_S$ . In other words, the only caustic in  $N_S$  is a fold arc passing through the origin.

By Taylor expanding, we see that the Jacobian matrix of the lensing map  $\vec{\eta}$  is given at the origin  $\vec{x} = 0$  by

$$[\text{Jac } \vec{\eta}](0) = \begin{bmatrix} 1-2\hat{a} & -\hat{b} \\ -\hat{b} & 1-2\hat{c} \end{bmatrix}, \quad (\text{A1})$$

where

$$\hat{a} = \frac{1}{2}\psi_{11}(0), \quad \hat{b} = \psi_{12}(0), \quad \hat{c} = \frac{1}{2}\psi_{22}(0). \quad (\text{A2})$$

The subscripts indicate partial derivatives of  $\psi$  relative to  $\vec{x} = (x_1, x_2)$ . Note that  $\psi$  has no linear part (since  $\vec{\eta}$  maps the origin to itself). For  $\vec{y} = 0$  to be fold caustic point, the rank of  $[\text{Jac } \vec{\eta}](0)$  must be unity, which means that we must have  $(1-2\hat{a})(1-2\hat{c})-\hat{b}^2=0$  while at least one of  $(1-2\hat{a})$ ,  $(1-2\hat{c})$ , and  $\hat{b}^2$  does not vanish (Petters et al. 2001, p. 349). Consequently,  $(1-2\hat{a})$  and  $(1-2\hat{c})$  cannot both vanish. We lose no generality by assuming  $1-2\hat{a} \neq 0$ .

Now introduce the orthogonal matrix (see Petters et al. 2001, p. 344)

$$\mathbf{M} = \frac{1}{\sqrt{(1-2\hat{a})^2 + \hat{b}^2}} \begin{bmatrix} 1-2\hat{a} & -\hat{b} \\ \hat{b} & 1-2\hat{a} \end{bmatrix}, \quad (\text{A3})$$

and define new orthogonal coordinates in the neighborhoods  $N_L$  and  $N_S$  by

$$\vec{\theta} = (\theta_1, \theta_2) \equiv \mathbf{M} \vec{x}, \quad \vec{u} = (u_1, u_2) \equiv \mathbf{M} \vec{y}. \quad (\text{A4})$$

(Note that the coordinate changes are the *same* in the lens and light source planes, which is different from the approach of Schneider et al. 1992, p. 185.) Using these coordinates, Petters et al. (2001, p. 346) showed rigorously that  $\vec{x} = 0$  is a fold critical point if and only if the following conditions hold:

$$(1-2\hat{a})(1-2\hat{c}) = \hat{b}^2, \quad 1-2\hat{a} \neq 0, \quad \hat{d} \equiv -\psi_{222}(0) \neq 0. \quad (\text{A5})$$

*Remark:* The matrix  $\mathbf{M}$  orthogonally diagonalizes  $[\text{Jac } \vec{\eta}](0)$ .

Let us now Taylor expand the lens potential near the origin. We argue below that carrying the expansion to fourth order in  $\vec{\theta}$  is both necessary and sufficient for the precision we desire. The most general fourth order expansion can be written as (see Petters et al. 2001, pp. 346–347)

$$\psi(\vec{\theta}) = \frac{1}{2}(1-K)\theta_1^2 + \frac{1}{2}\theta_2^2 + e\theta_1^3 + f\theta_1^2\theta_2 + g\theta_1\theta_2^2 + h\theta_2^3 + k\theta_1^4 + m\theta_1^3\theta_2 + n\theta_1^2\theta_2^2 + p\theta_1\theta_2^3 + r\theta_2^4. \quad (\text{A6})$$

The zeroth order term in the potential is irrelevant, so we neglect it. The first order terms must vanish in order to ensure that the origin of the lens plane maps to the origin of the source plane. In the second order terms, the coefficients of the  $\theta_1\theta_2$  and  $\theta_2^2$  terms are fixed (to 0 and 1/2, respectively) by the conditions that the origin is a fold critical point such that  $[\text{Jac } \vec{\eta}](0)$  is in diagonal form.

Conventional analyses of lensing near a fold caustic have only considered the  $K$ ,  $f$ ,  $g$ , and  $h$  terms in the expansion (e.g., Petters et al. 2001; Gaudi & Petters 2002a). However, we shall see below that some of the other terms are significant for our analysis.

## A.2. Image positions and magnifications

We seek to use perturbation theory (e.g., Bellman 1966) to find expansions for the image positions and magnifications that are accurate to first order in  $\vec{u}$ . We shall work from our fourth order expansion of the lens potential, and then verify that it is adequate for our purposes. For bookkeeping purposes, let us introduce scalar parameter  $\xi$  by taking  $\vec{u} \rightarrow \xi \vec{u}$ , so we can identify terms of a given order by examining the power of  $\xi$ .

For the potential eq. (A6), the lens equation is

$$\xi u_1 = K\theta_1 - (3e\theta_1^2 + 2f\theta_1\theta_2 + g\theta_2^2) - (4k\theta_1^3 + 3m\theta_1^2\theta_2 + 2n\theta_1\theta_2^2 + p\theta_2^3), \quad (\text{A7})$$

$$\xi u_2 = -(f\theta_1^2 + 2g\theta_1\theta_2 + 3h\theta_2^2) - (m\theta_1^3 + 2n\theta_1^2\theta_2 + 3p\theta_1\theta_2^2 + 4r\theta_2^3). \quad (\text{A8})$$

Since the lowest order terms are linear or quadratic in  $\vec{\theta}$ , it is natural to postulate that the image positions can be written as a series expansion in  $\xi$  with the following form:

$$\theta_1 = \alpha_1 \xi^{1/2} + \beta_1 \xi + \mathcal{O}(\xi)^{3/2}, \quad (\text{A9})$$

$$\theta_2 = \alpha_2 \xi^{1/2} + \beta_2 \xi + \mathcal{O}(\xi)^{3/2}, \quad (\text{A10})$$

Substituting into the lens equation, we obtain:

$$0 = (\alpha_1 K) \xi^{1/2} - (3\alpha_1^2 e + 2\alpha_1\alpha_2 f + \alpha_2^2 g - \beta_1 K + u_1) \xi + \mathcal{O}(\xi)^{3/2}, \quad (\text{A11})$$

$$0 = -(\alpha_1^2 f + 2\alpha_1\alpha_2 g + 3\alpha_2^2 h + u_2) \xi - [2\alpha_1\beta_1 f + 2(\alpha_1\beta_2 + \alpha_2\beta_1) g + 6\alpha_2\beta_2 h + \alpha_1^3 m + 2\alpha_1^2\alpha_2 n + 3\alpha_1\alpha_2^2 p + 4\alpha_2^3 r] \xi^{3/2} + \mathcal{O}(\xi)^2 \quad (\text{A12})$$

It is easily understood why these equations are carried to different orders. Eq. (A7) has a term that is linear in  $\vec{\theta}$ , which means that correction terms appear at  $\mathcal{O}(\xi)^{3/2}$ . By contrast, in eq. (A8) the lowest order term is quadratic in  $\vec{\theta}$ , and since

$$\theta_i \theta_j = \alpha_i \alpha_j \xi + (\alpha_i \beta_j + \alpha_j \beta_i) \xi^{3/2} + \mathcal{O}(\xi)^2 \quad (\text{A13})$$

we see that the correction terms only appear at  $\mathcal{O}(\xi)^2$ .

Following perturbation theory, we can now solve for the unknowns  $\alpha_i$  and  $\beta_i$  by demanding that eqs. (A11) and (A12) be satisfied at each order in  $\xi$ . We then find that the positions of the two images can be written as

$$\theta_1^\pm = \frac{3hu_1 - gu_2}{3hK} \xi + \mathcal{O}(\xi)^{3/2}, \quad (\text{A14})$$

$$\theta_2^\pm = \mp \sqrt{\frac{-u_2}{3h}} \xi^{1/2} - \frac{3ghu_1 - (g^2 + 2Kr)u_2}{9h^2K} \xi + \mathcal{O}(\xi)^{3/2}. \quad (\text{A15})$$

Note that the distance between the two images is

$$d_1 = 2 \sqrt{\frac{-u_2}{3h}} \xi^{1/2} + \mathcal{O}(\xi)^{3/2}. \quad (\text{A16})$$

To find the magnifications of the images, we compute the Jacobian determinant of the lens equation, and evaluate that at  $\vec{\theta}^\pm$  to obtain

$$(\mu^\pm)^{-1} = \pm 2K \sqrt{-3hu_2} \xi^{1/2} + \frac{4}{3h} (g^2 - 3fh + 2Kr) u_2 \xi + \mathcal{O}(\xi)^{3/2}. \quad (\text{A17})$$

This result shows that the  $\pm$  labels for the two images have been assigned such that  $\mu^+ > 0$  while  $\mu^- < 0$ .

*Remarks:* (1) To check our results, we note that at lowest order we recover the same scalings  $d_1 \propto \xi^{1/2}$  and  $\mu^\pm \propto \xi^{-1/2}$  found by previous analyses (Schneider et al. 1992; Petters et al. 2001; Gaudi & Petters 2002a). (2) To first order in  $\xi$  the image separation and the two magnifications depend only on the  $u_2$  component of the source position. (3) In several places we have  $\sqrt{-hu_2}$  or  $\sqrt{-u_2/h}$ . In general, at least for simple lens potentials like an isothermal ellipsoid or isothermal sphere with shear, we have  $h \leq 0$  all along the caustic. This means that only source positions with  $u_2 > 0$  lead to the production of two fold images.

At first order in the image positions and magnifications, the presence of  $r$  demonstrates that the fourth order terms in eq. (A6) cannot be ignored. At the same time, we can now verify that going to fourth order is sufficient. Any term of  $\mathcal{O}(\vec{\theta})^5$  in the potential would enter the lens equation at  $\mathcal{O}(\vec{\theta})^4$ ; that would in turn be of order  $\xi^2$  or higher, which is beyond the order to which we are working. Similarly, terms of  $\mathcal{O}(\vec{\theta})^5$  in the potential would enter  $\mu^{-1}$  at  $\mathcal{O}(\vec{\theta})^3$  or at least  $\xi^{3/2}$ . In other words, going to fourth order in eq. (A6) is both necessary and sufficient when we seek the image positions and magnifications correct to first order in  $\xi$ .

### A.3. Generic behavior of the fold relation

From eq. (A17) we see that the two fold images have magnifications that are equal and opposite to lowest order in  $\xi$ , which means that the combination  $|\mu^+| - |\mu^-|$  should approximately vanish. In observed lenses, the magnifications are not directly observable but the fluxes are, so to construct a dimensionless combination of the fluxes we define

$$R_{\text{fold}} \equiv \frac{|\mu^+| - |\mu^-|}{|\mu^+| + |\mu^-|} = \frac{F^+ - F^-}{F^+ + F^-}. \quad (\text{A18})$$

Plugging in the series expansions for  $\mu^\pm$ , we find

$$R_{\text{fold}} = \frac{2(g^2 - 3fh + 2Kr)}{3hK} \sqrt{\frac{-u_2}{3h}} \xi^{1/2} + \mathcal{O}(\xi). \quad (\text{A19})$$

By comparing the expansion for  $d_1$  in eq. (A16), we see that we can write

$$R_{\text{fold}} = A_{\text{fold}} d_1 + \mathcal{O}(\xi), \quad (\text{A20})$$

where

$$A_{\text{fold}} \equiv \frac{g^2 - 3fh + 2Kr}{3hK} = \frac{3\psi_{122}^2 - 3\psi_{112}\psi_{222} + \psi_{2222}(1 - \psi_{11})}{6\psi_{222}(1 - \psi_{11})}. \quad (\text{A21})$$

In the last equality, we have replaced the coefficients  $(f, g, h, K, r)$  with their definitions in terms of derivatives of the potential; for example,

$$f = \frac{1}{2} \psi_{112} = \frac{1}{2} \frac{\partial^3 \psi}{\partial \theta_1^2 \partial \theta_2}, \quad (\text{A22})$$

$$g = \frac{1}{2} \psi_{122} = \frac{1}{2} \frac{\partial^3 \psi}{\partial \theta_1 \partial \theta_2^2}, \quad (\text{A23})$$

and so forth, where the derivatives are evaluated at the origin  $\vec{\theta} = 0$ .

To summarize,  $R_{\text{fold}}$  vanishes for a source asymptotically close to a fold caustic. For a source a small but finite distance away, there is a correction term that scales as the square root of the distance of the source from the caustic, or (more usefully) as the separation between the two fold images. The coefficient  $A_{\text{fold}}$  of this linear scaling depends on properties of the lens potential at the fold critical point. In particular, the presence of  $r$  reiterates the fact that the fourth order expansion in the potential (eq. A6) is necessary to obtain an expansion for  $R_{\text{fold}}$  that is accurate at order  $\xi^{1/2}$  or  $d_1$ .

We have verified all of the approximations in this appendix by comparing them to exact numerical solutions of the lens equation obtained with the software by Keeton (2001).

## B. DATA FOR THE OBSERVED FOUR-IMAGE LENSES

In this appendix we summarize the observational data that we use for all of the observed four-image lenses; this text complements the data values given in Table 1. For each lens system, we need the relative positions of the lensed images in order to measure the separations  $d_1$  and  $d_2$ , and also to use as constraints on lens models for determining the Einstein radius  $R_{\text{ein}}$ . The position of the lens galaxy (or galaxies), if available, is also valuable for the lens modeling. We also need the flux ratios between the images in order to determine  $R_{\text{fold}}$ . We consider radio and optical/near-infrared flux ratios separately, because they are believed to

correspond to very different source sizes and provide very different information about small-scale structure in the lens potential (see, e.g., Dalal & Kochanek 2002; Dobler & Keeton 2005). At optical/near-infrared wavelengths, we examine the colors of the images to detect (and correct for) any differential extinction that may be present. Falco et al. (1999) carried out a detailed version of this analysis for a sample of lenses that includes seven that we consider, and we use their results where available. If there is no evidence for differential extinction, we combine data from different passbands using a weighted average. At radio wavelengths, we again examine the wavelength dependence of the flux ratios to determine that there are no significant electromagnetic effects. In three lenses (HE 0435–1223, WFI 2033–4723, and Q2237+0305) some additional flux ratio measurements are available, as discussed below.

**0047–2808:** This is a quadruply imaged system (Warren et al. 1996, 1999), but its lack of pointlike images means that it requires special modeling techniques (e.g., Wayth et al. 2004), and that it is probably not very interesting for the analysis of small-scale structure anyway. We do not include it in our sample.

**B0128+437:** For the image positions, we use the radio astrometry from Phillips et al. (2000). For the radio fluxes, we use the mean and scatter in  $R_{\text{fold}}$  from 41 epochs of MERLIN monitoring by Koopmans et al. (2003a). The monitoring shows no evidence for time dependence.

**HE 0230–2130:** We use the optical HST astrometry from CASTLES. There are two lens galaxies; we include both of them in lens models, taking their observed positions as constraints but optimizing their masses. For the optical fluxes of the lensed images, we use the BRI data for images A, B, and C from Wisotzki et al. (1999). The colors are consistent with no differential extinction. (Image D is not well separated from galaxy G2 in the Wisotzki et al. data, so we do not consider it.)

**MG 0414+0534:** We use the optical HST astrometry from CASTLES. We include the satellite galaxy near the lens galaxy (“object X” Schechter & Moore 1993) in lens models. For the optical image fluxes, we use the extinction-corrected flux ratios from Falco et al. (1999). For the radio fluxes, we use the high-resolution VLBI data from Trotter et al. (2000). Those observations resolve each image into four subcomponents; the  $R_{\text{fold}}$  values are similar for the different subcomponents, so we take the weighted average. The radio flux ratios are constant in time to 1–3% (Moore & Hewitt 1997).

**HE 0435–1223:** We use the optical HST astrometry from CASTLES. For the optical broad-band fluxes, we use the *gri* data from Wisotzki et al. (2002). Wisotzki et al. (2003) also report emission line fluxes; we take the mean and scatter in  $R_{\text{fold}}$  from the C IV and C III] lines. There is no evidence for wavelength dependence in the broad-band flux ratios, and the spectra of the different images have identical spectral slopes, so there does not appear to be any differential extinction. Image D appeared to vary by 0.07 mag between the two sets of observations, which may imply evidence for microlensing.

**B0712+472:** We use the optical HST astrometry and photometry from CASTLES. The values of  $R_{\text{fold}}$  differ slightly in the V, I, and H bands, but within the measurement uncertainties; hence there is no evidence for differential extinction. For the radio fluxes, we use the mean and scatter in  $R_{\text{fold}}$  from MERLIN monitoring by Koopmans et al. (2003a). There is evidence for time dependence in the radio fluxes.

**RX J0911+0551:** We use the optical HST astrometry and photometry from CASTLES. The lens galaxy has a satellite galaxy, which we include in lens models. The image flux ratios vary with wavelength in a manner that is consistent with differential extinction, so we correct for extinction using a redshifted  $R_V = 3.1$  extinction curve from Cardelli et al. (1989, also see Paper I).

**SDSS 0924+0219:** We use the ground-based astrometry and photometry from Inada et al. (2003). The *gri* colors are consistent with no differential extinction.

**SDSS 1004+4112:** This lens is produced by a cluster rather than a single galaxy (Oguri et al. 2004), but we can still treat it with our formalism. We use ground-based *griz* data from Oguri et al. (2004), and HST/I data from Inada et al. (2004). There is no evidence for differential extinction. Richards et al. (2004) claimed to observe microlensing of the broad emission lines in image A, but the level of variability in the continuum is not yet known.

**PG 1115+080:** We use the HST astrometry and photometry from CASTLES Falco et al. (1999) find that the VIH data are consistent with no differential extinction. In the lens models, we explicitly include the group of galaxies surrounding the lens (see Keeton & Kochanek 1997; Impey et al. 1998).

**RX J1131–1231:** We use the ground-based astrometry and photometry from Sluse et al. (2003). They report two epochs of V data and one epoch of R. The colors are consistent with no differential extinction. The total flux varied between the two epochs, but the flux ratios remained constant.

**HST 12531–2914:** We use the HST astrometry and photometry from Ratnatunga et al. (1995) and CASTLES. Falco et al. (1999) find that the V–I colors are consistent with no extinction (within the noise).

**HST 14113+5211:** We use the HST astrometry and photometry from Fischer et al. (1998) and CASTLES. There is some scatter among the values of  $R_{\text{fold}}$  obtained from V-, R-, and I-band data, but the scatter is within the (fairly large) measurement uncertainties.

**H1413+117:** We use the HST astrometry from CASTLES. For the optical fluxes, we use the extinction-corrected flux ratios from Falco et al. (1999).

**HST 14176+5226:** We use the HST astrometry and photometry from Ratnatunga et al. (1995). Falco et al. (1999) find that the colors are consistent with no differential extinction.

**B1422+231:** We use the radio data from Patnaik et al. (1999). The radio fluxes are basically constant in time (Patnaik & Narasimha 2001). For the optical fluxes, we use the extinction-corrected flux ratios from Falco et al. (1999).

**B1555+375:** We use the radio data from Marlow et al. (1999). The data from radio monitoring by Koopmans et al. (2003a) yield similar results, but have larger formal errors.

**B1608+656:** Fassnacht et al. (2002) monitored the radio fluxes, measured the time delays, and determined the delay-corrected magnification ratios; we take the mean and scatter in  $R_{\text{fold}}$  from their three seasons of data. There are two lens galaxies; we model the system using data from Koopmans et al. (2003b).

**B1933+503:** There are ten lensed images associated with three different sources. We use all of the images in lens modeling, following Cohn et al. (2001). However, for the fold analysis we use only the fold quad consisting of images 1/3/4/6. For the radio fluxes, we first take the mean and scatter from 8.4 GHz monitoring by Biggs et al. (2000), and then combine that in weighted average with measurements at other wavelengths by Sykes et al. (1998).

**WFI 2026–4536:** We use the optical data from Morgan et al. (2004a). We use all available data in which the images are resolved:  $ugriHK_s$  plus HST/F160W for images B and C; and  $iHK_s$  plus HST/F160W for images  $A_1$  and  $A_2$ . There is some wavelength dependence that may suggest differential extinction or microlensing, the current data are inconclusive. We simply take the mean and scatter in  $R_{\text{fold}}$  from all of the data.

**WFI 2033–4723:** We use the optical data from Morgan et al. (2004a). For the optical broad-band flux ratios, we use all available data in which the images are resolved:  $ugri$  for images B and C; and  $ri$  for images  $A_1$  and  $A_2$ . Morgan et al. also report emission line flux ratios; we take the weighted average of  $R_{\text{fold}}$  from the C IV, C III], and Mg II lines.

**B2045+265:** We use the radio positions from Fassnacht et al. (1999). For the radio fluxes, we combine various measurements by Fassnacht et al. (1999) and monitoring by Koopmans et al. (2003a), and take the mean and scatter in  $R_{\text{fold}}$ . For the optical fluxes, we use HST data from CASTLES for images A, B, and C (image D was not detected). The VIH colors are consistent with no differential extinction.

**Q2237+0305:** We use HST astrometry from CASTLES. For the broad-band optical fluxes, we use the microlensing light curves from Woźniak et al. (2000). We correct for differential extinction using the reddening deduced by Falco et al. (1999). For the radio fluxes, we use the data from Falco et al. (1996). In addition, Agol et al. (2000) report mid-infrared flux ratios measured at  $8.9\ \mu\text{m}$  and  $11.7\ \mu\text{m}$ .

## REFERENCES

Agol, E., Jones, B., & Blaes, O. 2000, *ApJ*, 545, 657  
 Amara, A., Metcalf, R. B., Cox, T. J., & Ostriker, J. P. 2004, *astro-ph/0411587*  
 Bellman, R. 1966, Perturbation Techniques in Mathematics, Engineering and Physics (Mineola: Dover)  
 Bender, R., Surma, P., Döbereiner, S., Möllenhoff, C., Madejski, R. 1989, *A&A*, 217, 35  
 Bernstein, G., Fischer, P., Tyson, J. A., & Rhee, G. 1997, *ApJ*, 483, L79  
 Biggs, A. D., Xanthopoulos, E., Browne, I. W. A., Koopmans, L. V. E., & Fassnacht, C. D. 2000, *MNRAS*, 318, 738  
 Bradač, M., Schneider, P., Lombardi, M., Lombardi, M., King, L. J., & Porcas, R. 2002, *A&A*, 388, 373  
 Bradač, M., Schneider, P., Lombardi, M., Steinmetz, M., Koopmans, L. V. E., & Navarro, J. F. 2004, *A&A*, 797, 809  
 Cardelli, J. A., Clayton, G. C., & Mathis, J. S. 1989, *ApJ*, 345, 245  
 Chen, J., Kravtsov, A. V., & Keeton, C. R. 2003, *ApJ*, 594, 24  
 Chiba, M. 2002, *ApJ*, 565, 17  
 Cohn, J. D., Kochanek, C. S., McLeod, B. A., & Keeton, C. R. 2001, *ApJ*, 554, 1216  
 Dalal, N. 1998, *ApJ*, 509, L13  
 Dalal, N., & Kochanek, C. S. 2002, *ApJ*, 572, 25  
 Dalal, N., & Watson, C. R. 2004, *astro-ph/0409483*  
 Dobler, G., & Keeton, C. R. 2005, *astro-ph/0502436*  
 Evans, N. W., & Hunter, C. 2002, *ApJ*, 575, 68  
 Evans, N. W., & Witt, H. J. 2003, *MNRAS*, 345, 1351  
 Falco, E. E., Lehár, J., Perley, R. A., Wambsganss, J., & Gorenstein, M. V. 1996, *AJ*, 112, 897  
 Falco, E. E., et al. 1999, *ApJ*, 523, 617  
 Fassnacht, C. D., et al. 1999, *AJ*, 117, 658  
 Fassnacht, C. D., Xanthopoulos, E., Koopmans, L. V. E., & Rusin, D. 2002, *ApJ*, 581, 823  
 Fischer, P., Schade, D., & Barrientos, L. P. 1998, *ApJ*, 503, L127  
 Fluke, C. J., & Webster, R. L. 1999, *MNRAS*, 302, 68  
 Gaudi, B. S., & Petters, A. O. 2002a, *ApJ*, 574, 970  
 Gaudi, B. S., & Petters, A. O. 2002b, *ApJ*, 580, 468  
 Heyl, J. S., Hernquist, L., & Spergel, D. N. 1994, *ApJ*, 427, 165  
 Holder, G., & Schechter, P. 2003, *ApJ*, 589, 688  
 Hunter, C., & Evans, N. W. 2001, *ApJ*, 554, 1227  
 Impey, C. D., et al. 1998, *ApJ*, 509, 551  
 Inada, N., et al. 2003, *AJ*, 126, 666  
 Inada, N., et al. 2004, *PASJ*, submitted  
 Jørgensen, I., Franx, M., & Kjærgaard, P. 1995, *MNRAS*, 273, 1097  
 Keeton, C. R. 2001, *astro-ph/0102340*  
 Keeton, C. R. 2003, *ApJ*, 584, 664  
 Keeton, C. R., Gaudi, B. S., & Petters, A. O. 2003, *ApJ*, 598, 138 (Paper I)  
 Keeton, C. R., & Kochanek, C. S. 1997, *ApJ*, 487, 42  
 Keeton, C. R., Kochanek, C. S., & Seljak, U. 1997, *ApJ*, 482, 604  
 Keeton, C. R., et al. 2000, *ApJ*, 542, 74  
 Keeton, C. R., & Winn, J. N. 2003, *ApJ*, 590, 39  
 Keeton, C. R., & Zabludoff, A. I. 2004, *ApJ*, 612, 660  
 Klypin, A., Kravtsov, A. V., Valenzuela, O., & Prada, F. 1999, *ApJ*, 522, 82  
 Kochanek, C. S. 1991, *ApJ*, 373, 354  
 Kochanek, C. S. 2004, 605, 58  
 Kochanek, C. S., & Dalal, N. 2004, *ApJ*, 610, 69  
 Koopmans, L. V. E., et al. 2003a, *ApJ*, 595, 712  
 Koopmans, L. V. E., et al. 2003b, *ApJ*, 599, 70  
 Marlow, D. R., et al. 1999, *AJ*, 118, 654  
 Mao, S. 1992, *MNRAS*, 389, 63  
 Mao, S., & Schneider, P. 1998, *MNRAS*, 295, 587  
 Mao, S., Jing, Y., Ostriker, J. P., & Weller, J. 2004, *ApJ*, 604, L5  
 Metcalf, R. B. 2004a, *astro-ph/0407298*  
 Metcalf, R. B. 2004b, *astro-ph/0412538*  
 Metcalf, R. B., & Madau, P. 2001, *ApJ*, 563, 9  
 Metcalf, R. B., & Zhao, H. 2002, *ApJ*, 567, L5  
 Metcalf, R. B., Moustakas, L. A., Bunker, A. J., & Parry, I. R. 2004, *ApJ*, 607, 43  
 Möller, O., Hewett, P., & Blain, A. W. 2003, *MNRAS*, 345, 1  
 Moore, B., Ghigna, S., Governato, F., Lake, G., Quinn, T., Stadel, J., & Tozzi, P. 1999, *ApJ*, 524, L19  
 Moore, C. B., & Hewitt, J. N. 1997, *ApJ*, 491, 451  
 Morgan, N. D., et al. 2004a, *AJ*, 127, 2617  
 Morgan, N. D., Kochanek, C. S., Pevunova, O., & Schechter, P. L. 2004b, *astro-ph/0410614*  
 Moustakas, L. A., & Metcalf, R. B. 2003, *MNRAS*, 339, 607  
 Naab, T., & Burkert, A. 2003, *ApJ*, 597, 893  
 Oguri, M., & Lee, J. 2004, *MNRAS*, 355, 120  
 Oguri, M., et al. 2004, *ApJ*, 605, 78  
 Patnaik, A. R., Kemball, A. J., Porcas, R. W., & Garrett, M. A. 1999, *MNRAS*, 307, L1  
 Patnaik, A. R., & Narasimha, D. 2001, *MNRAS*, 326, 1403  
 Petters, A. O., Levine, H., & Wambsganss, J. 2001, Singularity Theory and Gravitational Lensing (Boston: Birkhäuser)  
 Phillips, P. M., et al. 2000, *MNRAS*, 319, L7  
 Quadri, R., Möller, O., & Natarajan, P. 2003, *ApJ*, 597, 659  
 Ratnatunga, K., Ostrander, E. J., Griffiths, R. E., & Im, M. 1995, *ApJ*, 453, L5  
 Rest, A., van den Bosch, F. C., Jaffe, W., Tran, H., Tsvetanov, Z., Ford, H. C., Davies, J., & Schafer, J. 2001, *AJ*, 121, 2431  
 Richards, G. T., et al. 2004, *ApJ*, 610, 679  
 Rusin, D., & Tegmark, M. 2001, *ApJ*, 553, 709  
 Rusin, D., et al. 2001, *ApJ*, 557, 594  
 Saglia, R. P., Bender, R., & Dressler, A. 1993, *A&A*, 279, 75  
 Saha, P., & Williams, L. L. R. 2003, *AJ*, 125, 2769  
 Schechter, P. L., & Moore, C. B. 1993, *AJ*, 105, 1  
 Schechter, P. L., & Wambsganss, J. 2002, *ApJ*, 580, 685  
 Schechter, P. L., Udalski, A., Szymański, M., Kubiak, M., Pietrzyński, G., Soszyński, I., Woźniak, P., Żelębiński, K., Szewczyk, O., & Wyrzykowski, Ł. 2003, *ApJ*, 584, 657  
 Schneider, P., Ehlers, J., & Falco, E. E. 1992, Gravitational Lenses (Berlin: Springer)  
 Schneider, P., & Weiss, A. 1992, *A&A*, 260, 1  
 Sluse, D., et al. 2003, *A&A*, 406, L43  
 Sykes, C. M., et al. 1998, *MNRAS*, 301, 310  
 Trotter, C. S., Winn, J. N., & Hewitt, J. N. 2000, *ApJ*, 535, 671

Warren, S. J., Hewett, P. C., Lewis, G. F., Møller, P., Iovino, A., & Shaver, P. A. 1996, MNRAS, 278, 139

Warren, S. J., Lewis, G. F., Hewett, P. C., Møller, P., Shaver, P. A., & Iovino, A. 1999, A&A, 343, L35

Wayth, R. B., Warren, S. J., Lewis, G. F., & Hewett, P. C. 2004, astro-ph/0410253

Wayth, R. B., O'Dowd, M., & Webster, R. L. 2005, astro-ph/0502396

Winn, J. N., Kochanek, C. S., Keeton, C. R., & Lovell, J. E. J. 2003, ApJ, 590, 26

Wisotzki, L., Christleib, N., Liu, M. C., Maza, J., Morgan, N. D., & Schechter, P. L. 1999, A&A, 348, L41

Wisotzki, L., Schechter, P. L., Bradt, H. V., Heinmüller, J., & Reimers, D. 2002, A&A, 395, 17

Wisotzki, L., Becker, T., Christensen, L., Helms, A., Jahnke, K., Kelz, A., Roth, M. M., & Sanchez, S. F. 2003, A&A, 408, 455

Witt, H. J., & Mao, S. 1997, MNRAS, 291, 211

Witt, H. J., & Mao, S. 2000, MNRAS, 311, 689

Woźniak, P. R., Alard, C., Udalski, A., Szymański, M., Kubiak, M., Pietrzyński, G., & Zebrun, K. 2000, ApJ, 529, 88

Yoo, J., Kochanek, C. S., Falco, E. E., & McLeod, B. A. 2005, astro-ph/0502299

Zentner, A. R., & Bullock, J. S. 2003, ApJ, 598, 49

TABLE B1. LENS DATA

	Image Pair	$d_1$	$R_{\text{fold}}$ (optical)	$R_{\text{fold}}$ (radio)	$R_{\text{fold}}$ (other)	References
B0128+437 $R_{\text{ein}} = 0.20$ fold	AB	0.14		0.263 $\pm$ 0.023		Koopmans et al. (2003a)
	AD	0.27		0.328 $\pm$ 0.028		
	CD	0.42		0.014 $\pm$ 0.042		
	CB	0.50		-0.058 $\pm$ 0.037		
HE0230-2130 $R_{\text{ein}} = 0.82$ fold	AB	0.74	0.000 $\pm$ 0.008			Wisotzki et al. (1999)
	CD	1.46				
	AD	1.64				
	CB	1.65	-0.289 $\pm$ 0.007			
MG0414+0534 $R_{\text{ein}} = 1.08$ fold	A <sub>1</sub> A <sub>2</sub>	0.41	-0.024 $\pm$ 0.038	0.085 $\pm$ 0.002		Falco et al. (1999), Trotter et al. (2000)
	BA <sub>2</sub>	1.71	-0.500 $\pm$ 0.043	-0.477 $\pm$ 0.004		
	A <sub>1</sub> C	1.96	0.739 $\pm$ 0.015	0.736 $\pm$ 0.003		
	BC	2.13	0.400 $\pm$ 0.046	0.323 $\pm$ 0.007		
HE0435-1223 $R_{\text{ein}} = 1.18$ cross	CB	1.53	-0.029 $\pm$ 0.014		-0.035 $\pm$ 0.010	Wisotzki et al. (2002), Wisotzki et al. (2003)
	AB	1.59	0.226 $\pm$ 0.004		0.136 $\pm$ 0.005	
	CD	1.85	0.049 $\pm$ 0.019		0.137 $\pm$ 0.007	
	AD	1.88	0.299 $\pm$ 0.012		0.300 $\pm$ 0.011	
B0712+472 $R_{\text{ein}} = 0.68$ fold/cusp	AB	0.17	0.519 $\pm$ 0.052	0.085 $\pm$ 0.036		Koopmans et al. (2003a), CASTLES
	CB	0.91	-0.123 $\pm$ 0.075	-0.337 $\pm$ 0.051		
	CD	1.18	0.361 $\pm$ 0.062	0.672 $\pm$ 0.120		
	AD	1.25	0.636 $\pm$ 0.062	0.848 $\pm$ 0.060		
RXJ0911+0551 $R_{\text{ein}} = 0.95$ cusp	BA	0.48	0.027 $\pm$ 0.013			CASTLES
	BC	0.62	0.303 $\pm$ 0.012			
	DC	2.96	-0.137 $\pm$ 0.016			
	DA	3.08	-0.400 $\pm$ 0.014			
SDSS0924+0219 $R_{\text{ein}} = 0.87$ fold	AD	0.74	0.861 $\pm$ 0.005			Inada et al. (2003)
	AC	1.19	0.428 $\pm$ 0.009			
	BD	1.37	0.704 $\pm$ 0.010			
	BC	1.53	0.038 $\pm$ 0.014			
SDSS1004+4112 $R_{\text{ein}} = 6.91$ fold	AB	3.73	0.194 $\pm$ 0.015			Oguri et al. (2004), Inada et al. (2004)
	DB	11.44	-0.512 $\pm$ 0.017			
	AC	11.84	0.401 $\pm$ 0.011			
	DC	14.38	-0.312 $\pm$ 0.016			
PG1115+080 $R_{\text{ein}} = 1.03$ fold	A <sub>1</sub> A <sub>2</sub>	0.48	0.215 $\pm$ 0.011			CASTLES
	A <sub>1</sub> B	1.67	0.722 $\pm$ 0.009			
	CB	1.99	0.214 $\pm$ 0.019			
	CA <sub>2</sub>	2.16	-0.445 $\pm$ 0.011			
RXJ1131-1231 $R_{\text{ein}} = 1.81$ cusp	BA	1.19	0.209 $\pm$ 0.013			Sluse et al. (2003)
	CA	1.26	-0.272 $\pm$ 0.019			
	BD	3.14	0.824 $\pm$ 0.012			
	CD	3.18	0.587 $\pm$ 0.026			
HST12531-2914 $R_{\text{ein}} = 0.55$ cross	BC	0.77	-0.092 $\pm$ 0.057			Ratnatunga et al. (1995), CASTLES
	AC	0.78	-0.187 $\pm$ 0.046			
	BD	0.91	0.164 $\pm$ 0.089			
	AD	1.02	0.015 $\pm$ 0.078			
HST14113+5211 $R_{\text{ein}} = 0.83$ cross	CD	1.13	0.138 $\pm$ 0.049			Fischer et al. (1998), CASTLES
	CB	1.38	0.287 $\pm$ 0.109			
	AD	1.41	0.128 $\pm$ 0.049			
	AB	1.42	0.305 $\pm$ 0.116			
H1413+117 $R_{\text{ein}} = 0.56$ cross	AB	0.76	0.031 $\pm$ 0.016			Falco et al. (1999)
	AC	0.87	0.205 $\pm$ 0.015			
	DC	0.91	-0.056 $\pm$ 0.023			
	DB	0.96	-0.229 $\pm$ 0.022			
HST14176+5226 $R_{\text{ein}} = 1.33$ cross	CB	1.73	0.088 $\pm$ 0.040			Ratnatunga et al. (1995)
	AB	2.09	0.163 $\pm$ 0.040			
	CD	2.13	0.089 $\pm$ 0.043			
	AD	2.13	0.164 $\pm$ 0.040			
B1422+231 $R_{\text{ein}} = 0.76$ cusp	AB	0.50	-0.038 $\pm$ 0.018	-0.038 $\pm$ 0.007		Falco et al. (1999), Patnaik et al. (1999)
	CB	0.82	-0.317 $\pm$ 0.020	-0.339 $\pm$ 0.006		
	AD	1.25	0.942 $\pm$ 0.019	0.936 $\pm$ 0.006		
	CD	1.29	0.898 $\pm$ 0.032	0.884 $\pm$ 0.011		
B1555+375 $R_{\text{ein}} = 0.24$ fold	AB	0.09		0.274 $\pm$ 0.003		Marlow et al. (1999), Koopmans et al. (2003a)
	CB	0.35		-0.084 $\pm$ 0.004		
	AD	0.40		0.858 $\pm$ 0.006		
	CD	0.42		0.725 $\pm$ 0.010		
B1608+656 $R_{\text{ein}} = 0.77$ fold	AC	0.87		0.321 $\pm$ 0.006		Fassnacht et al. (2002)
	BC	1.51		-0.016 $\pm$ 0.002		
	AD	1.69		0.706 $\pm$ 0.004		
	BD	2.00		0.486 $\pm$ 0.004		
B1933+503 $R_{\text{ein}} = 0.49$ fold	4-3	0.46		0.656 $\pm$ 0.007		Sykes et al. (1998), Biggs et al. (2000)
	4-6	0.63		0.637 $\pm$ 0.007		
	1-3	0.90		0.143 $\pm$ 0.014		
	1-6	0.91		0.111 $\pm$ 0.013		
WFI2026-4536 $R_{\text{ein}} = 0.65$ fold	A <sub>1</sub> A <sub>2</sub>	0.33	0.181 $\pm$ 0.043			Morgan et al. (2004a)
	A <sub>1</sub> C	0.83	0.626 $\pm$ 0.015			
	BC	1.19	-0.431 $\pm$ 0.014			
	BA <sub>2</sub>	1.28	0.096 $\pm$ 0.011			

TABLE B1. LENS DATA—Continued

Image Pair	$d_1$	$R_{\text{fold}}$ (optical)	$R_{\text{fold}}$ (radio)	$R_{\text{fold}}$ (other)	References
WFI2033-4723 $R_{\text{ein}} = 1.06$ fold	A <sub>1</sub> A <sub>2</sub>	0.72	0.219 ± 0.010	0.174 ± 0.099	Morgan et al. (2004a)
	A <sub>1</sub> C	1.54	0.330 ± 0.007	0.056 ± 0.074	
	BA <sub>2</sub>	2.01	-0.072 ± 0.012	-0.042 ± 0.091	
	BC	2.13	0.077 ± 0.044	-0.161 ± 0.057	
B2045+265 $R_{\text{ein}} = 1.13$ cusp	AB	0.28	0.255 ± 0.017	0.287 ± 0.020	Fassnacht et al. (1999), CASTLES
	CB	0.56	0.153 ± 0.023	0.133 ± 0.045	
	AD	1.91		0.809 ± 0.022	
	CD	1.93		0.750 ± 0.033	
Q2237+0305 $R_{\text{ein}} = 0.85$ cross	AD	1.01	(variable; see text)	0.130 ± 0.145	-0.008 ± 0.068
	BD	1.18		0.172 ± 0.139	0.048 ± 0.062
	AC	1.37		0.289 ± 0.170	0.270 ± 0.079
	BC	1.40		0.328 ± 0.163	0.319 ± 0.072

NOTE. — The lengths  $R_{\text{ein}}$  (Column 1) and  $d_1$  (Column 3) are given in arcseconds. We do not explicitly quote  $d_2$ , because it can be determined from the other  $d_1$  values. For example, in B0128+437 the value of  $d_2$  for image pair AB would be the smaller of  $d_1(\text{AD})$  and  $d_1(\text{CB})$ . CASTLES denotes the CfA/Arizona Space Telescope Lens Survey (see <http://cfa-www.harvard.edu/castles>).